AERODYNAMICS OF WINGS AT LOW REYNOLDS NUMBERS

by

John McArthur

A Qualifying Exam Proposal Presented to the

FACULTY OF THE GRADUATE SCHOOL

UNIVERSITY OF SOUTHERN CALIFORNIA

In Partial Fulfillment of the

Requirements for the Degree

DOCTOR OF PHILOSOPHY

(AEROSPACE AND MECHANICAL ENGINEERING)

July 2007

Contents

List of Figures

Chapter 1

Introduction

1.1 Motivation

Due to advances in energy, actuator, and sensor technologies, it is possible to build small scale flying devices with mean wing chords of 5 cm flying at about 10 m/s. Lithium batteries have energy and power densities that far exceed Nickel-Metal Hydride batteries and can be made very small; muscle wire and magnet-coil actuators are lighter and smaller than traditional servo actuators; and cameras and chemical sensors have decreased dramatically in size and weight due to advances in electronics. Aircraft at this size and speed could have many uses in military reconnaissance, traffic monitoring, search and rescue, and forest fire detection. [26]

Planes similar to these have been built and flown for nearly a decade, starting with the Black Widow built by Aerovironment, and continuing with others, including universities that compete in the annual Micro Air Vehicle (MAV) competition. [12] However, these flying vehicles still have small endurance and range compared to other flying vehicles, are quite inefficient, and have low payload to airframe weight ratios. Hence, they are not widely used. These planes could prove to be useful if these characteristics were improved.

To improve the endurance, range, efficiency and payload capacity of these vehicles, one could look to lighter materials, higher energy density power systems, high efficiency power systems, or the aerodynamics of the vehicle. This thesis concerns the lift and drag

generated by the fluid dynamics of particular airfoil shapes for the air vehicles described above.

A useful non-dimensional parameter in the study of aerodynamics is the Reynolds number (Re). This can be seen in the non-dimensional form of the Navier-Stokes equations, which are the equations that govern fluid motion. For an incompressible, Newtonian fluid, these equations have the form:

$$\frac{\partial \mathbf{u}}{\partial t} + (\mathbf{u} \cdot \bigtriangledown)\mathbf{u} = \bigtriangledown p + \frac{1}{\mathrm{Re}} \bigtriangledown^2 \mathbf{u} \tag{1.1}$$

where $\bigtriangledown$ is the spatial gradient operator normalized by some length scale (L), $\mathbf{u}$ is the velocity vector normalized by some velocity scale (U), t is the time normalized by the convective time scale ($\frac{\mathrm{L}}{\mathrm{U}}$), p is the pressure normalized by the dynamic pressure ($\rho \mathrm{U}^2$), and ρ is the fluid density. With these normalizations, the Re is defined as:

$$\mathrm{Re} = \frac{\rho \mathrm{UL}}{\mu}$$

where μ is the fluid viscosity. Since the numerator of the Reynolds number is composed of mass, velocity and size, and the denominator consists of viscosity, the Reynolds number can be thought of as the ratio of inertial forces to viscous forces in the flow. When viscosity is dominant, the flow is laminar and smooth because viscosity distributes and transports momentum throughout the flow. This is seen in equation 1.1 because when viscosity is dominant, then the Re will be small. With sufficiently small Re, the LaPlacian term on the right will govern the fluid dynamics, and the non-linear term on the left will not significantly effect the flow. Laminar flows, with the limit Re approaching zero, can often be solved analytically, and computational solutions can be found with direct simulations of the Navier-Stokes equations. When inertial forces dominate the flow, then the flow is turbulent and disorganized because local increases in momentum

cause instability. This is seen in equation 1.1 because with dominant inertial forces the Re will be large, thus the non-linear terms on the left will start to influence the dynamics. At sufficiently high Re, the non-linear terms dominate, and the fluid is considered fully turbulent. Direct simulations of turbulent flows are computationally expensive and are currently not practical for aircraft design. However, many approximations of the characteristics of turbulent flow have been developed, and these can be implemented in computational algorithms to get solutions that are close enough to experimental results to be useful. The use of these approximations has led to great advances in the design and performance of large, high-speed aircraft that operate at high Re.

As an example of laminar and turbulent flow, a flat plate boundary layer has an Re that can be defined by the free-stream flow speed (U_∞) and the distance along the plate (x). Thus:

$$\mathrm{Re}_x = \frac{\rho \mathrm{U}_\infty x}{\mu}$$

As the boundary layer travels along the plate, the Re increases. For Re $< 3 \times 10^6$, the boundary layer is laminar, but when Re $> 4 \times 10^6$, the boundary layer is considered fully turbulent. Thus, $3 \times 10^6 <$ Re $< 4 \times 10^6$ is a transition region where there is neither laminar flow nor turbulent flow. [33] In this region, direct simulation of the Navier-Stokes equations are typically too time consuming to be used, and conventional turbulence models will not accurately predict the fluid dynamics.

When looking at wings and airfoils, the situation is similar, but there are some differences. The main difference is the existence of a pressure gradient on the upper surface of the airfoil which effects the transitional Re. Defining an Re for an airfoil based on the airfoil chord (c) gives:

$$\mathrm{Re}_\mathrm{c} = \frac{\rho \mathrm{U}_\infty \mathrm{c}}{\mu}$$

While this is the Re for the airfoil, the local Re can still be considered to be the distance along the chord from the leading edge of the airfoil. When $\mathrm{Re_c} > 10^6$, most of the boundary layer on the wing is turbulent, and the laminar and transitional regions have relatively little effect on the forces on the wing. Thus, computations can use approximations and models for the turbulent boundary layer and get adequate results. When $\mathrm{Re_c} < 10^3$, there will be so much viscosity that the flow over typical airfoils will not transition to turbulence, and the flow can be solved with direct simulation. Thus, $10^3 < \mathrm{Re_c} < 10^6$ is a transitional region for airfoils and wings. It is the region where laminar, transitional and turbulent flow all have a significant effect on the forces generated by the wing, and each must be modeled accurately.

1.2 Nomenclature

Throughout this paper, the Re based on the chord (c), typically denoted $\mathrm{Re_c}$, will simply be referred to as the Re. The chord line of a wing is the line that connects the trailing edge to the leading edge. The angle that this line makes with the free-stream velocity is the geometric angle of incidence, and will be referred to as α in this paper. The span from wing-tip to wing-tip will be denoted b, and the aspect ratio (b/c) will be referred to as A.

The stream-wise direction is x, the span-wise direction is y, and the direction perpendicular to both x and y (the vertical) is z. The velocity components in each of these three directions is (u, v, w), respectively.

The lift drag coefficient are the forces normalized by the dynamic pressure ($\frac{1}{2}\rho \mathrm{U_\infty}^2$) multiplied by the projected area of the wing (cb). These coefficients are denoted as C_L and C_D for finite aspect ratio wings, and C_l and C_d for 2D-infinite aspect ratio wings. They are only functions of the shape of the wing, and the Re of the wing.

1.3 Low Reynolds Number Aerodynamics

The earliest rigorous study of aerodynamics within this range of Re was conducted by Schmitz during the 1930's. [34] Using a wind tunnel, he measured the forces generated by airfoils in the range $2 \times 10^4 <$ Re $< 2 \times 10^5$. He focused his study on three airfoil shapes: a thin flat plate, a thin cambered plate, and a thick cambered airfoil (the N60). His studies showed that the thick cambered airfoil has a critical Re where the performance changes drastically. Figure 1.1 is a plot of his results for the N60 airfoil across a range of Re. In this plot, the lift coefficient and drag coefficient are called c_a and c_w, respectively (the German convention). Above the critical Re range, the lift-to-drag ratio is much higher than below. This critical Re range is similar to the transitional Re range described above for a flat plate boundary layer. When an airfoil is below its critical Re range, the flow is dominated by viscous forces and remains laminar over the entire airfoil. Above this range, the flow will transition to turbulence somewhere on the airfoil.

Over the next few decades, Schmitz's results were verified and expanded upon by Abbott [2], Riegels [32], and Althaus [4]. For most airfoil sections, the critical Reynolds number is in the range 10^4 - 10^6. [24] By plotting the lift-to-drag ratios of airfoils across this range of Reynolds number, McMasters generalized these results in 1979 with a wide band as shown in figure 1.2.

McMasters' plot shows that, in general, smooth airfoils have a higher lift-to-drag ratio than rough airfoils at high Re. Thus, roughness causes a decrease in performance at Re above approximately 10^5. However, below this Re, roughness is beneficial. Smooth airfoils have a large decrease in lift-to-drag ratio, while rough airfoils perform nearly as well as they did at the higher Re.

Building off this information, Mueller conducted both visualization and force measurement experiments to understand the cause for this performance decrease at low Re. [25] His studies focused on measuring the lift and drag forces on the NACA 66_3-018

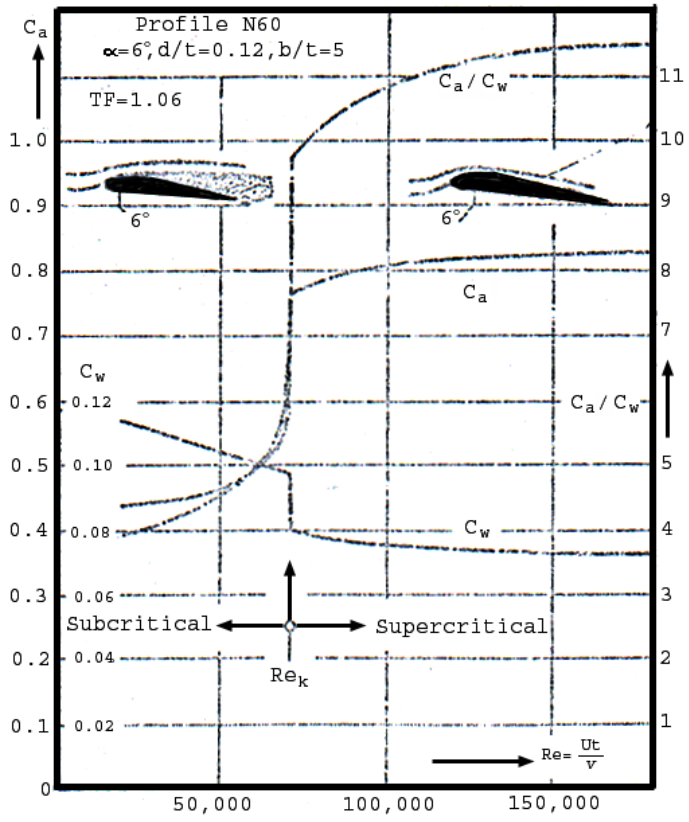

Figure 1.1: The critical Re (Schmitz)
The maximum lift and minimum drag coefficient (C_a and C_w) of the N60 airfoil across its critical Re. The sudden lift increase and drag decrease as Re increases past the critical value are caused by the boundary layer transition. [34]

airfoil at $4 \times 10^4 <$ Re $< 4 \times 10^5$. This is a symmetric airfoil that is 18% thick. Due to the limitations of his force balance (minimum resolvable force of 10 mN), the drag force measurements were only made at Re $> 10^5$. The lift measurements made at Re $= 4 \times 10^4$ show a dramatic change at $\alpha \approx 8\,\mathrm{deg}$, as shown in figure 1.3(a). At Re $> 10^5$ however, the lift coefficient was found to increase linearly with α (as it does at all larger Re). Using smoke visualization, Mueller showed that the drastic increase in lift coefficient found at Re $= 4 \times 10^4$ and $\alpha \approx 8\,\mathrm{deg}$ is due to the formation of a Laminar Separation Bubble at that angle of attack. This bubble will be described in section

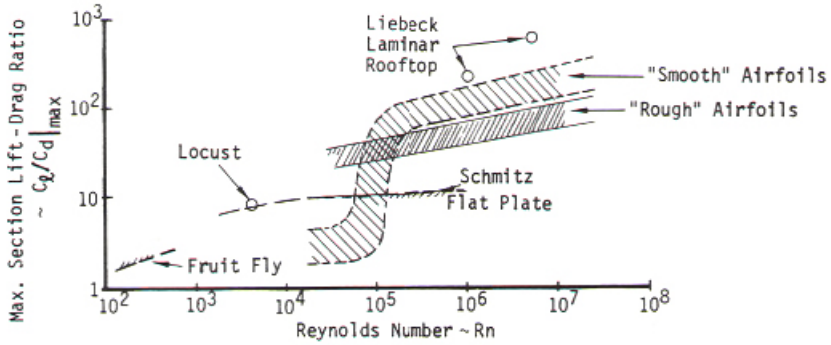

Figure 1.2: Maximum Lift-to-Drag vs Reynolds number (McMasters)
This plot is a generalization of the performance of many airfoils to qualitatively describe what happens as Re decreases. The data is taken from Jacobs and Sherman[16], Schmitz [34], Abbott and von Doenhoff [1], Riegels [32], Althaus [4], and Hoerner [15]. The figure was made by McMasters and is a summary of their data. [24]

1.3, but for now it is sufficient to note that this measurement is made at Re $= 4 \times 10^4$, which is in the range indicated by the McMasters plot as a region where smooth airfoils experience a decrease in performance. It seems likely that the decrease in performance as Re decreases explained by McMasters is related in some way to the formation of the discontinuity in the lift vs angle of attack plot shown by Mueller.

This finding by Mueller should not be interpreted to contradict the results of Schmitz and the other plotted in McMaster's generalization. Instead, it is a more detailed understanding of how the forces generated by an airfoil change as Re enters the critical Re of the airfoil. For the same airfoil, Mueller measured the lift coefficient at Re $= 4 \times 10^5$, and that is shown in figure 1.3(b). The lift coefficient is much higher at this larger Re than at the lower Re of 4×10^4, consistent with the previous findings.

Another series of extensive airfoil studies at low Re was conducted by Selig starting in 1986 at Princeton University. In this study, lift and drag were measured for 60 airfoils primarily at $6 \times 10^4 <$ Re $< 3 \times 10^5$. [35] The lift was measured directly using a strain-gauge force balance, while the drag was estimated by the wake deficit measured by a

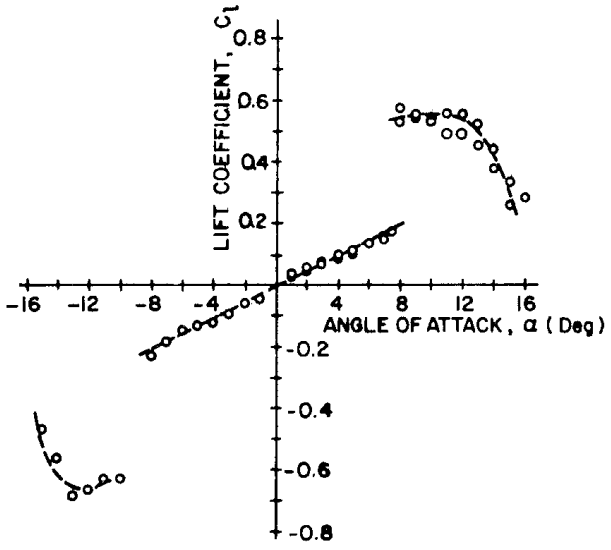

(a) Re $= 4 \times 10^4$

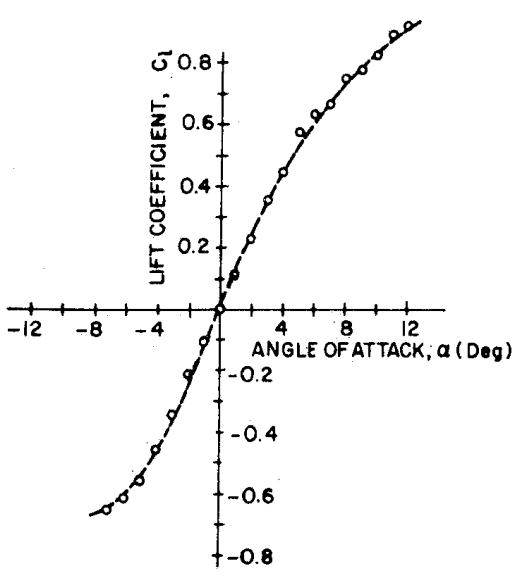

(b) Re $= 4 \times 10^5$

Figure 1.3: Lift curves for NACA 66_3-018 airfoil (Mueller)
End plates were used to measure 2D airfoil performance. The sudden increase in lift at $\alpha \approx 8°$ and Re $= 4 \times 10^4$ might be related to the change in performance indicated in figure 1.2. The same airfoil at much higher Re has much larger lift coefficients, consistent with the findings of Schmitz. [25]

pitot tube traversed vertically through the wake. The experiments were primarily concerned with improving the endurance and range of sail planes (non-powered airplanes) that operate in this range of Re.

The data obtained in this study showed that at Re $> 1 \times 10^5$, each airfoil has a drag polar that is qualitatively similar to drag polars at all higher Re. That is, the drag coefficient is low for a large range of lift coefficients. However, as Re decreases below this number, many of the airfoils have a significant increase in drag coefficient at moderate lift coefficients, while the drag coefficient at low and high lift coefficients is relatively low. This is seen in figure 1.4, where the drag polar for the Eppler 387 (E387) airfoil, as measured by various facilities, is plotted across a range of Re.

The plot in figure 1.4 is the result of carefully scanning in many plots of previous data, digitizing the points on those plots, then plotting them all together. The E387 airfoil is chosen for comparisons because it has been studied by more researchers at these Re than other airfoils. It is also a championship airfoil at sail plane competitions. It was designed by Richard Eppler to have a very high lift-to-drag ratio at Re $\approx 5 \times 10^5$. [38]

The two most interesting features of figure 1.4 are that there is more disagreement at the lowest Re and that, despite this disagreement, there is a consistent, qualitative change in the shape of the curve at the lowest Re. At $6 \times 10^4 <$ Re $< 3 \times 10^5$, the drag polars for this airfoil are qualitatively similar to the other airfoils in this study in that the minimum drag coefficient steadily increases as Re decreases. The drag coefficient increase at moderate lift coefficients seen at Re $= 6 \times 10^4$ was primarily seen only for thick, cambered airfoils, similar to the E387. A comparison of drag polars obtained at different facilities, like figure 1.4, shows that data obtained at the lowest Re are less repeatable than data obtained at higher Re. This is true for 3 main reasons. 1) The forces measured

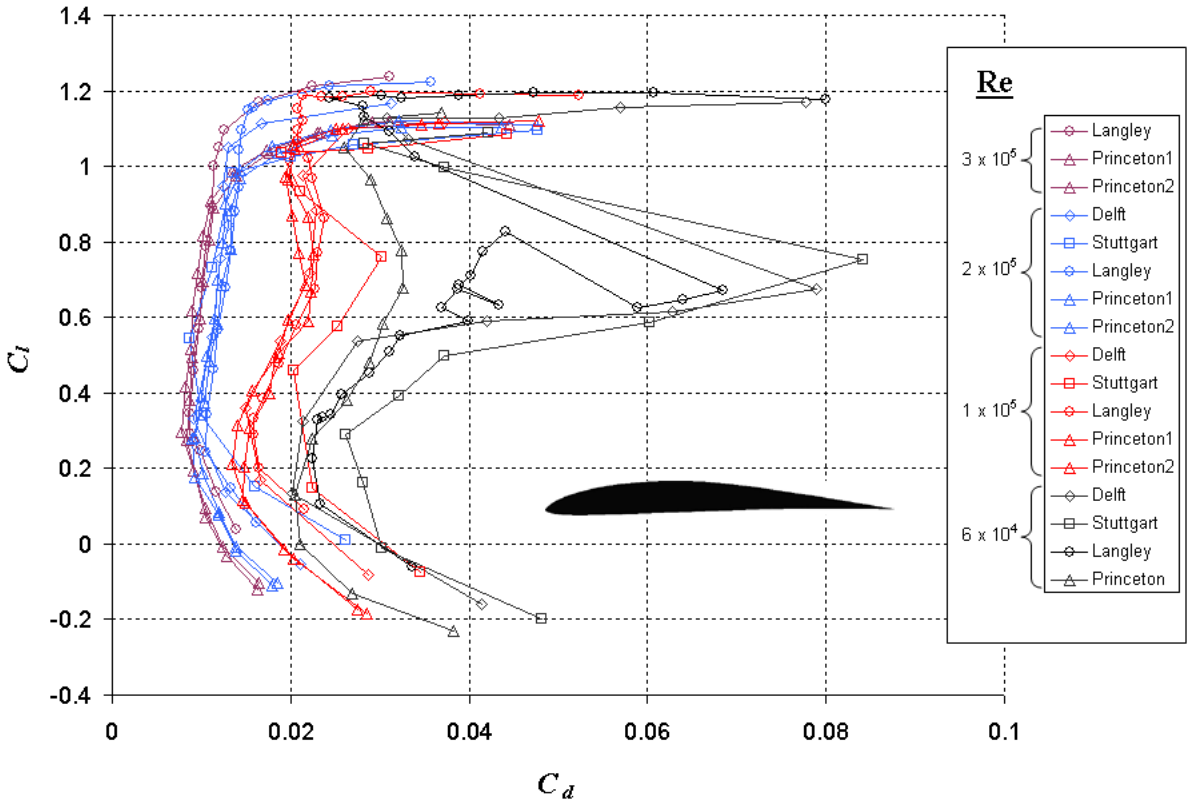

Figure 1.4: Drag polar of Eppler 387 airfoil at various Re
The drag polar of the E387 airfoil at $6 \times 10^4 < \text{Re} < 3 \times 10^5$ as measured by different facilities. The shape of the E387 airfoil is also shown. This is a collection of results from many sources that has been digitized and re-plotted here. [35] [36] [3] [23] [41]

here are much smaller than the higher Re, thus the relative uncertainty in the measurement is much higher. 2) The forces generated are much more sensitive to free-stream turbulence, surface roughness, and model geometry. 3) Different measurement techniques can return different results. Determining which explanation is most important is difficult, especially since none of the facilities report their measurement uncertainty. Reporting the measurement uncertainty can eliminate explanation 1 as being a dominant factor, but without the measurement uncertainties, the significance of the disagreement cannot be quantified.

Explanation 2 is typically assumed to be the most important factor in explaining the large disagreements. It is known that free-stream turbulence above 0.1% of the free-stream effects the transition process of a flat-plate boundary layer. [33] Also, the relative length of the transition region (relative to the chord length) increases as the chord-based Re of the airfoil approaches the critical Re. Thus, the effect of the transition region is more significant as the Re approaches the critical Re. Thus, when comparing experiments with different turbulence levels, the effect will show up in the experiments conducted at Re closer to the critical Re range of the airfoil. For the E387, the critical Re range has not been identified, but it is assumed to be around 6×10^4.

The final explanation is often discussed in the literature as well, but it is generally not considered to be as important as the explanation 2. There are primarily two ways to measure the drag of an airfoil: directly with a force balance, or indirectly by measuring the wake and estimating the force using the conservation of momentum. The difference between the two is that the wake can only be measured at discrete points along the span, and then there must be some assumption about the points that are not measured in order to get an estimate of the drag of the whole wing. However, at Re $\approx 10^5$, Selig et al showed that the wake is highly three-dimensional and it has much span-wise variation. [37] Figure 1.5 shows the wake deficit measured at different spanwise locations by Selig et al. The measurement shows the considerable spanwise variation described above, and this is at a relatively low angle of attack, and higher Re than the 6×10^4 case. No data is supplied for lower Re, but the variations most likely increase with decreasing Re.

Thus, many measurements of the wake would need to be made across the span to measure the drag of the wing accurately. At first, it would seem the direct force balance method would be obviously better than the indirect wake measurement method. However, when measuring airfoil performance experimentally, one must typically use end plates at the wing-tips of a finite span model. Pelletier and Mueller found that at low

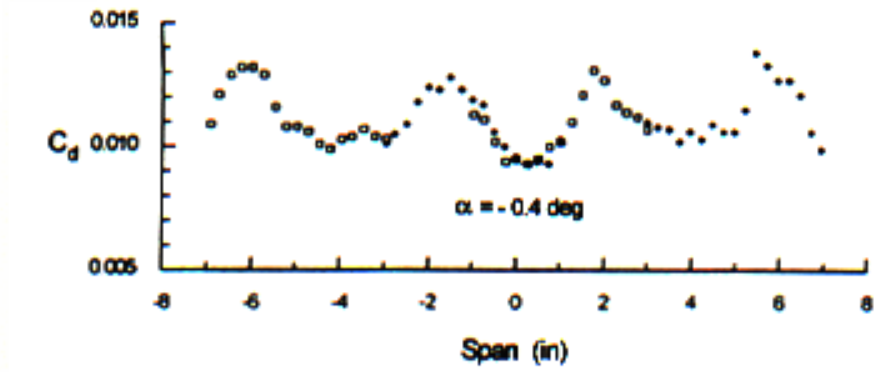

Figure 1.5: Wake deficit vs spanwise location at Re $= 2 \times 10^5$ (Selig)
Wake deficit drag coefficient estimate plotted against the spanwise location of the wake measurement. This is for the Eppler 374 airfoil at $\alpha = -0.4°$ and Re $= 2 \times 10^5$.[37]

Re, these end plates cause significant changes in the forces generated when compared to a true 2D airfoil. [29] Figure 1.6 shows the drag coefficient plotted against Reynolds number for the Eppler 61 airfoil at $\alpha = 0°$. The "3-piece airfoil" is a much better approximation of a true 2D airfoil than the other cases plotted. The data by Althaus and de Vries was taken using a wake measurement at the center-plane of the airfoil with end plates. Pelletier and Mueller found that end plates cause a 15% increase in drag and a 30% decrease in lift across this range of Re. The data also indicate that without sufficient sampling of the wake across the span, wake deficit measurements can yield unreliable drag estimates at this range of Re.

At sufficiently high Re, these two techniques yield very similar results, and compare well to computational results. Thus, using either of these techniques for airfoil force measurements is adequate at high Re. At Re in the current range of interest, neither technique is fully correct. However, the direct force measurement seems to have a systematic correction across all Re, while the indirect wake measurement method has no method of estimating possible errors.

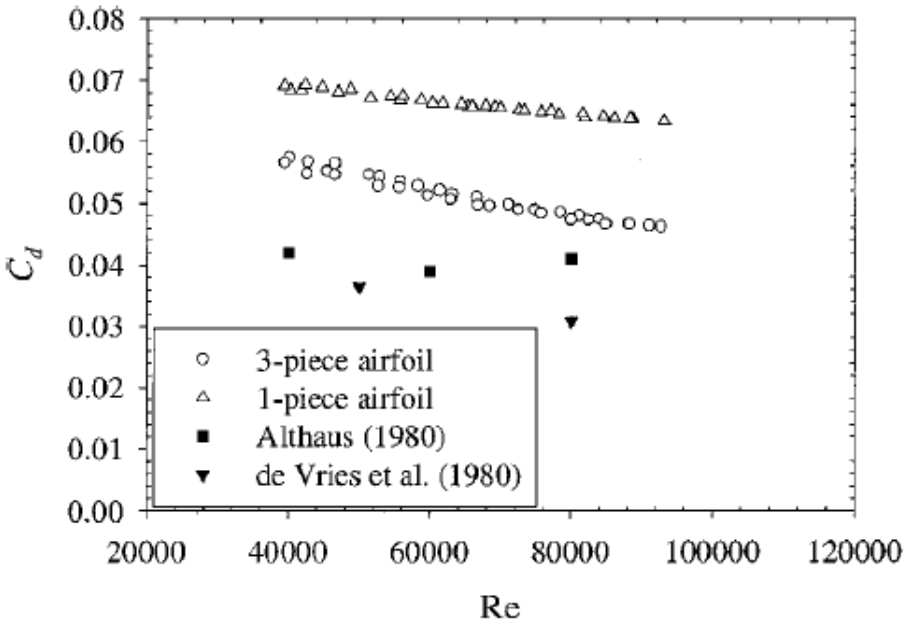

Figure 1.6: Drag coefficient vs Re for Eppler 61 airfoil (Mueller)
The drag coefficient of the E61 airfoil at $\alpha = 0^\circ$ as measured directly with a force balance by Mueller et al. The "3-piece airfoil" does not have end plate effects, and is therefore a much better approximation of a 2D airfoil while the "1-piece airfoil" has end plates at the wing tip. The Althaus and de Vries data were obtained by wake deficit measurements in the center of the wing with end plates used. It appears that end plates cause a systematic increase in measured drag, and that wake deficit measurements may yield incorrect drag estimates at these Re. [29]

Using a highly sensitive force balance, Laitone acquired some of the most reliable data on forces generated by low Re wings. [18] In fact, he claimed that his data is the first and only reliable force measurements at Re $< 10^5$ because his force balance has an uncertainty of $\pm$ 0.1 mN while Schmitz's was $\pm$ 1 mN and Mueller's was $\pm$ 10 mN. In addition, Laitone's wind tunnel had much lower turbulence levels ($\approx 0.02\%$). Laitone measured the lift and drag of a thin wedge (which approximated a flat plate), a 5% cambered plate, and the NACA 0012 at angles of attack from zero lift to well beyond stall. The range of Re was 2×10^4 - 7×10^4 and he demonstrated a variety of results that are peculiar to this range of Re. The first is that at Re $\approx 2 \times 10^4$, the 5% cambered

plate achieves the highest lift-to-drag ratio, while the NACA 0012 had the lowest, even lower than a simple thin wedge. This is shown in figure 1.7. In addition to these peculiar findings, figure 1.8 shows that the NACA 0012 has a higher lift coefficient when it is placed backwards in the flow, that is, when the trailing edge is used as the leading edge. These results indicate that a small leading edge radius is preferred at this range of Re.

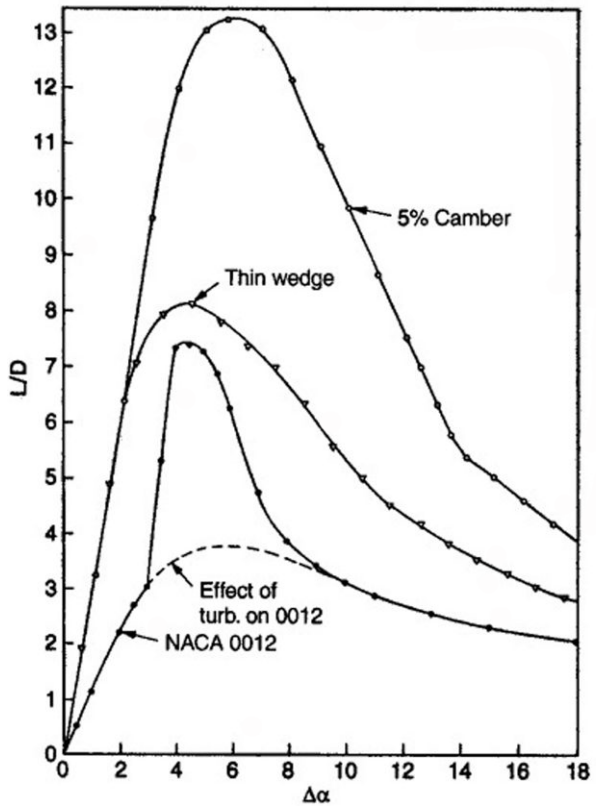

Figure 1.7: Lift to Drag ratio for three airfoil shapes (Laitone)
Data is taken for a thin-wedge (which approximates a flat-plate), a cambered plate, and the NACA 0012 airfoil at Re $\approx 2 \times 10^4$. The dashed line indicates the effect of a large increase in free-stream turbulence (close to the value present in Schmitz's experiments) on the NACA 0012 airfoil. [18]

He also found that a moderate increase of free-stream turbulence from 0.02% to 0.1% causes the NACA 0012 airfoil to have higher lift coefficients and higher lift-to-drag ratios. Much larger increases in free-stream turbulence (near the values in Schmitz's

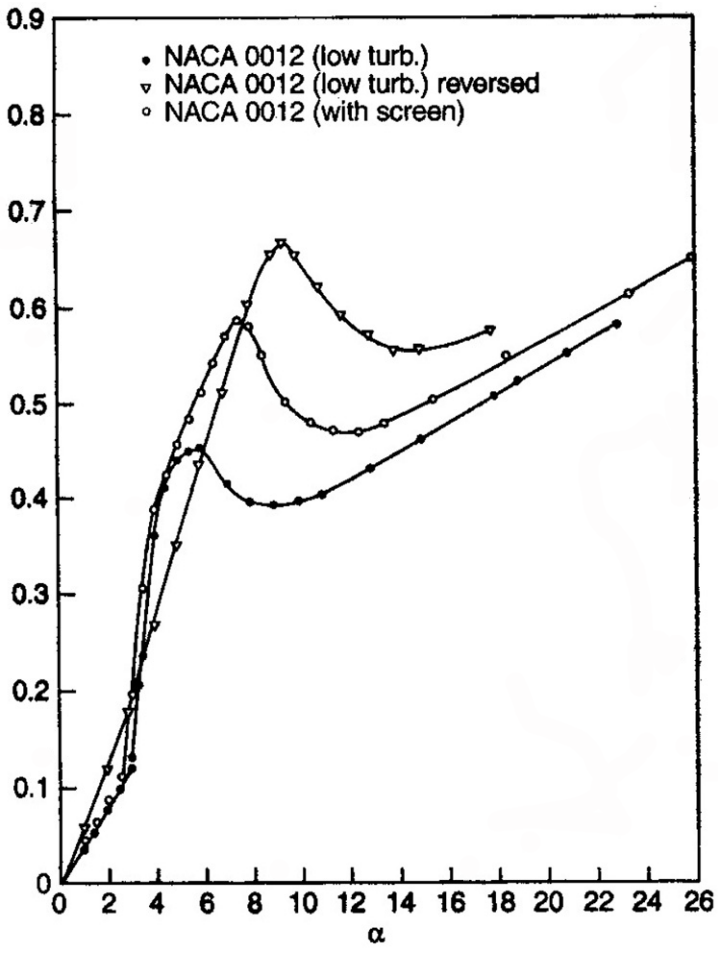

Figure 1.8: Lift curve for NACA 0012 (Laitone)
The lift coefficient vs angle of attack at Re $\approx 2 \times 10^4$. The "low turb" case is at 0.02% turbulent while the "with screen" case is at 0.10% turbulence. [18]

wind tunnel) cause the NACA 0012 to have much lower lift coefficients and lift-to-drag ratios. His overall conclusion is that at Re $< 5 \times 10^5$, potential flow theories do not apply because, the measured lift curve slopes at these Re are 20% larger than those predicted by Prandtl's lifting line theory. In addition, the induced drag coefficient is dependent on airfoil shape and Re.

Experiments at Re $< 5 \times 10^5$ were also conducted by Grundy et al. [13] They measured the forces of the Eppler 61 airfoil (5% thick, 5% camber) at Re = 2.5, 3.5, 5,

and 6×10^4. The tests were conducted in a wind tunnel with turbulence levels of 0.1% - 0.3%. Considering that Schubauer and Skramstad found the flat plate transition Re to be effected by free-stream turbulence levels of 0.1% and higher [33], the measurements of Grundy et al are likely to be effected by the turbulence level in their wind tunnel. In addition, the force balance used is rather insensitive in comparison to that used by Laitone. Grundy et al used a force balance with a resolution of $\pm$ 1 mN while Laitone's was $\pm$ 0.1 mN.

Despite these possible limitations, Grundy et al were able to find similarity between their force measurements and measurements made at Stuttgart, Delft and Notre Dame. They found the drag coefficient increases at moderate lift coefficients (similar to that shown above for the E387 airfoil), and their values of drag and lift coefficients were within reasonable agreement with previous measurements. They also measured a large degree of hysteresis in their force measurements depending on whether α was increasing or decreasing. This hysteresis depended on the noise levels present in the wind tunnel, and this was the focus of their studies, to measure the effect of single frequency acoustic disturbances on force generation from wings at these low Re. It was found that certain frequencies of acoustic excitation in the wind tunnel would cause a decrease in hysteresis.

One unexpected result of the research was in finding an additional explanation for the large discrepancy between measurements made at different facilities. Not only must the different turbulence values be accounted for, but also the different wind tunnel resonances of the experiments. The work of Grundy et al showed that since airfoil performance at $2 \times 10^4 <$ Re $< 6 \times 10^4$ is dependent on acoustic excitation, and since each wind tunnel resonates at a different frequency, it is quite likely that different wind tunnels will measure different performance in this range of Re, simply because of the different resonant frequencies..

Experiments conducted by Pelletier and Mueller measured both 2D airfoil performance as well as the performance of 3D rectangular planform wings.[28] They used a wind tunnel with a turbulence level of 0.05% and measured forces generated by a thin flat-plate wing (1.3% thick, 0% camber) and a thin cambered-plate wing (1.3% thick, 4% camber) at $6 \times 10^4 < \text{Re} < 2 \times 10^5$. They used end plates to measure approximate 2D conditions, and removed one of the end plates to measure approximate 3D conditions. Force measurements were made using a strain gauge force balance with a minimum measurable load of 10 mN, similar to Mueller's previous work in 1982. One of the results of this study was that, unlike the study by Grundy et al, no hysteresis was found. It is not clear whether this is caused by the decreased thickness of the wings, or by the decreased turbulence levels in the free-stream. Also, in contrast to the results of Laitone, potential flow theory seems to adequately predict the lift curve slope for the 3D wings studied at these Re.

1.4 Laminar Separation Bubble

The most common explanation for the unusual behavior of airfoils and wings at these low Re ($10^4 < \text{Re} < 10^5$) is the existence of a laminar separation bubble (LSB) at certain α. Selig claims that the LSB causes the peculiar drag increase at moderate lift coefficients. Grundy et al explain the hysteresis in their polars, and the large sensitivity to single frequency sound waves, on the LSB. And finally, Pelletier and Mueller state that the lack of hysteresis in their data is related to the lack of an LSB.

An LSB is demonstrated in figure 1.9. It typically begins with a laminar boundary layer that encounters an adverse pressure gradient, which causes the boundary layer to separate. The laminar separated shear flow is unstable and transitions to a turbulent separated shear flow. The turbulence then transports momentum from the free-stream,

across the shear layer, and down towards the surface. When the momentum transport is sufficient, the turbulent boundary layer is considered to be reattached to the surface, thus closing the separation bubble.[21]

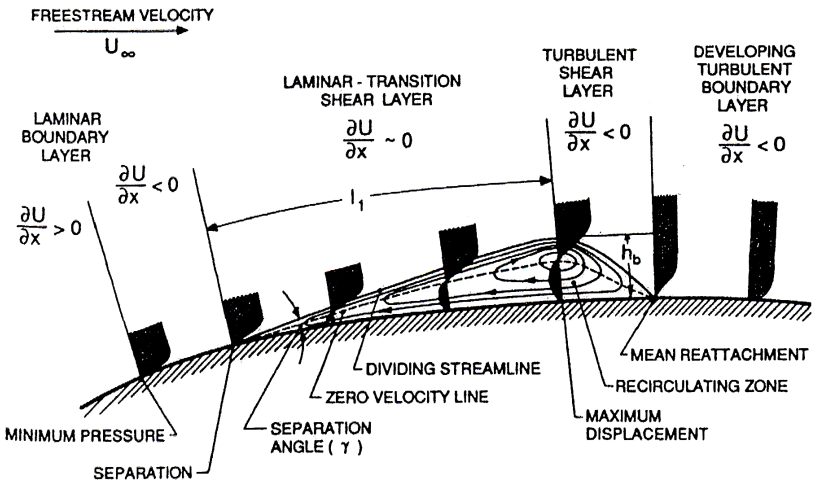

Figure 1.9: Description of a laminar separation bubble. (Mueller)
A schematic of the major features of a laminar separation bubble. The boundary layer is initially laminar, and separates just after the point of minimum pressure. The separated shear layer is much more unstable than an attached boundary layer and will transition to turbulence more quickly. Turbulent flows are able to transport momentum across the mean flow, and turbulent reattachment occurs downstream of the transition point. [6]

According the Selig et al, this LSB is responsible for the drag coefficient increase at moderate lift coefficients when the Eppler 387 airfoil is at Re $\approx 6 \times 10^4$ (see figure 1.4). He states on page 54 of Airfoils at Low Speed [35] that "The effects of a laminar separation bubble are apparent only at an Re of 60k through the mid-lift range, where the drag coefficient reaches a maximum of 0.032 at a [lift coefficient] of 0.5". Selig et al call this drag increase the "bubble drag" because it is caused by the LSB. [22] However, none of his studies at that time had investigated the boundary layer of the airfoils tested, and thus no direct evidence of this conclusion can be found.

Later tests by Selig et al used surface oil flow visualization techniques to discern the existence and size of the laminar separation bubble. [22] [38] This technique is used to visualize the time-averaged flow properties near the surface. With it, one can distinguish steady-state laminar and turbulent flow regions, separation/reattachment points, and the transition regions of a boundary layer. The tests conducted clearly show that there is a laminar separation point, and that there is a turbulent reattachment point. However, data were only shown for the relatively high Re of 2×10^5 and 3×10^5. [38] The drag polar of the airfoil at these Re show no sign of a drag coefficient increase at moderate lift coefficients (see figure 1.4). The "bubble drag" is only discernable for Re $\leq 1 \times 10^5$, an Re at which surface oil flow visualization is not available.

Selig et al claim that the LSB is responsible for the drag coefficient increase at moderate lift coefficients. However, there were no flow field measurements of the boundary layer to support such findings, only surface oil flow visualizations. Further, there were no flow measurements at all for the airfoil at Re $\leq 1 \times 10^5$, where the drag increase is most apparent.

A detailed review of the literature shows that there is no other support for this interpretation of the "bubble drag" either. Grundy et al claim that the increase in drag at moderate lift coefficients is associated with a "long separation bubble", while the decrease in drag as lift increases is associated with a transition in the flow from a long separation bubble to a short separation bubble. No measurements of the boundary layer are presented to support this claim. [13]

Laitone makes no mention of an LSB in his experiments on a flat plate, a cambered plate, and the NACA0012 airfoil at $2 \times 10^4 <$ Re $< 7 \times 10^4$. [18] Meanwhile, Pelletier and Mueller find no LSB in their experiments on thin flat and cambered plates at $6 \times 10^4 <$ Re $< 2 \times 10^5$. Using hydrogen bubbles in a water channel, they found that at all angles of attack there was no reattachment after the laminar separation. This seems

to explain the lack of hysteresis found in their results, and the lack of drag increase at moderate lift coefficients. [28] However, there is still limited understanding of whether or not the LSB actually causes the hysteresis or the drag decrease at moderate lift coefficients.

Many studies have focused on understanding the LSB, but they typically do not study the effect of the LSB on the forces generated by the wing. Also, many studies of the LSB are focused on a very small range of α, conditions where there is no drag increase at moderate lift coefficients, and geometries that have little significance to real planes.

Arena and Mueller studied the LSB formed by an airfoil with a cylindrical leading edge, followed by a constant thickness section, followed by a linearly tapered trailing edge. The LSB formed near the leading edge, just after the cylindrical section, and was measured by use of pressure taps on the upper surface, surface oil flow visualization, and smoke visualization. The study looked at $-4^\circ < \alpha < 6^\circ$, and $1.5 \times 10^5 <$ Re $< 4.5 \times 10^5$. [5] This study showed that as Re decreases across this range, the LSB increases in size from approximately 10% of the chord, to nearly 20%. As angle of incidence increases, the bubble also increases in size. They also point out the inherent difficulties in measuring the location and size of the unsteady bubble. The use of time-average techniques may be inappropriate, and averages of instantaneous measurements may be skewed due to inadequate sampling. These topics were not discussed in their reports of the experiments.

Broeren and Bragg conducted detailed studies of the LSB at low Re and related the LSB to the stall type. [7] At Re $= 3 \times 10^5$, they measured the time -dependent growth and decay of the LSB on the upper surface of the LRN(1)-1007 airfoil at $\alpha = 15^\circ$. The measurements were made using 2-component Laser Doppler Anemometry, with measurements made within 0.2 mm of the surface. The airfoil at this angle of incidence is 2° below the stall angle, and there are very large fluctuations in the forces generated

at this angle of attack. By measuring the flow field around the wing, they found a time period nature of the LSB: the LSB started small, then grew until it reached the trailing edge causing full separation, then suddenly became small again.

In a later paper, they relate this growth to the force fluctuations, and show that the dominant frequency of the fluctuating LSB is the same as that of the fluctuating lift force. [8] They also classified airfoils at this Re as having 5 common types of stall, and that each stall type was associated with a different amount of lift fluctuation near stall. The 5 stall types are: Trailing Edge, Leading Edge, Trailing Edge/Leading Edge, Thin Airfoil, and Thin Airfoil/Trailing Edge. The last two have an LSB that in some way causes the stall, either by growing until it reaches the trailing edge, or by growing until it reaches the point of trailing edge separation. These types of stall have the highest lift fluctuations near stall, with the combination Thin Airfoil/Trailing Edge stall having higher lift fluctuations than the pure Thin Airfoil stall.

A detailed comparison between time-averaged measurements of an LSB was done by Ol et al. [27] Experiments were performed at 3 facilities: a tow tank at the Institute for Aerospace Research, a wind tunnel at the Technical University of Braunschweig, and a water channel at the Air Force Research Lab. Each facility used PIV to measure the flow field around the SD7003 airfoil at $\alpha = 4\,\mathrm{deg}$ and Re $= 6\times10^4$. The resolution of the PIV system was adequate to resolve the boundary layer, and hence the LSB that is present at this angle of incidence. While there is an LSB for this airfoil at these conditions, and while it is at an Re $< 10^5$, the drag polar of the SD7003 has no characteristic "bubble drag" such as the E387 shown in figure 1.4. The drag polar of this airfoil, as found in reference [36], is shown in figure 1.10 at various Re, including the one investigated by Ol et al. It seems that the LSB measured by Ol et al does not cause a drag increase at moderate lift coefficients. Thus the separation bubble is having very little effect on

the shape of the drag polar of the airfoil, and may not be the explanation for the drag increase at moderate lift coefficients found for the E387 at Re $= 6 \times 10^4$.

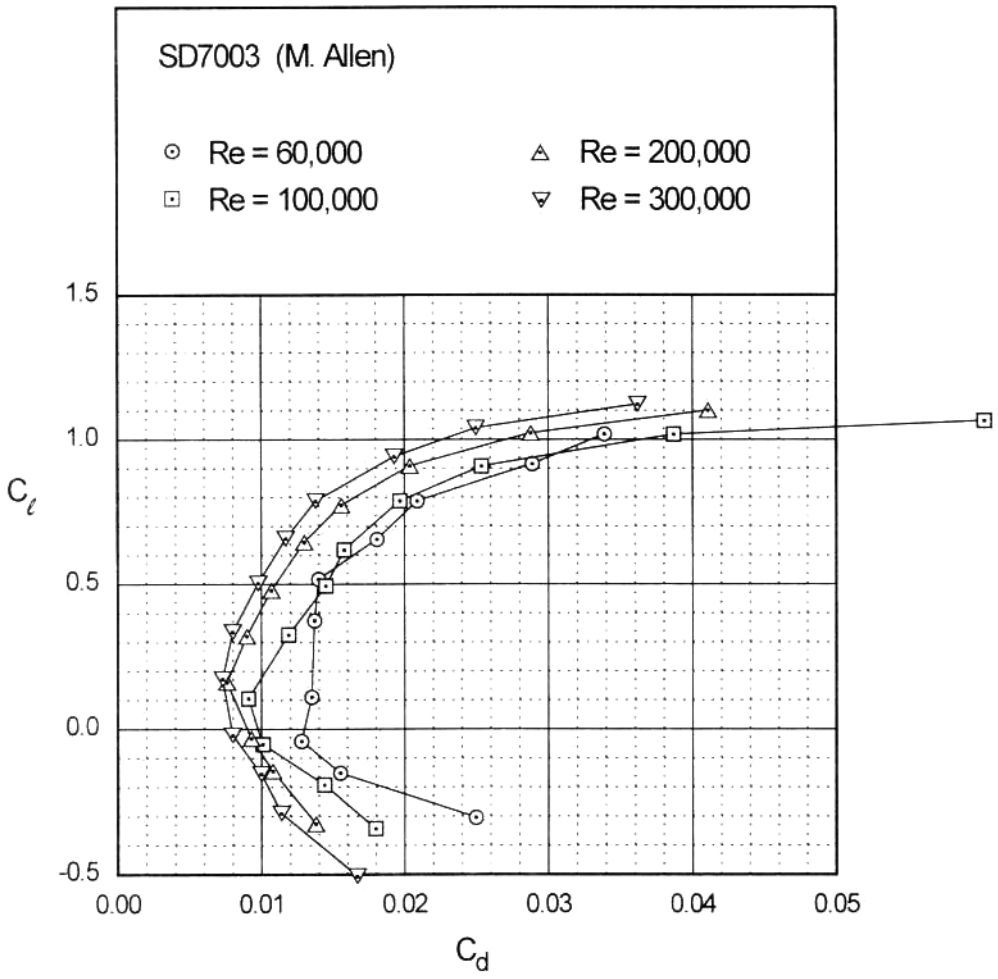

Figure 1.10: Drag polar of a SD7003 airfoil at various Re. (Selig)
The drag polar at the lowest Re shows no sign of the so called "bubble drag" which should cause a dramatic drag increase at moderate lift coefficients. [36]

While good agreement in LSB size and location was found between the facilities compared by Ol et al, measurements were only made at one angle of incidence and one Re. This yields little insight on how the bubble grows and how it effects the forces

generated by the wing. Also, no force measurements were made, and it is not clear how the LSB effects the forces generated by the airfoil.

Computational techniques are also being used to investigate the LSB at low Re. In the above study by Ol et al, they compared Xfoil results to their measurements of the LSB. Xfoil computes the flow around an airfoil by first computing the potential flow on a grid around the airfoil using a panel method, then it solves the boundary layer equations at points along the airfoil. The largest positive amplification rate of waves for each boundary layer profile is calculated and integrated along the surface. The integration of the amplification rates (referred to as the N-value) has been experimentally correlated to the point of transition to turbulence, and there is a critical N-value at which transition to turbulence occurs. For most cases, the critical N-value is 9. Thus, with some assumptions and some correlations, one can compute the external flow, the boundary layer profile along the surface, and the transition to turbulence. After transition, turbulence models can be used to model the flow. Unfortunately, Xfoil only computes the flow near the surface and the forces on the wing. Thus, the recirculating flow can not be verified by plotting velocity fields. However, by plotting the local skin friction coefficient of the wing, Xfoil can indicate a region of reverse flow, which would identify the location of an LSB. This is shown in figure 1.11 as a plot of skin friction vs location along the upper surface of the SD7003 airfoil. Laminar separation occurs when the skin friction becomes negative, and turbulent reattachment occurs when it becomes positive again.

The results of Xfoil showed an LSB at approximately the same location as the measurements, but no quantitative uncertainty analysis was made and it is unclear how accurate the Xfoil results will be in various other cases. In addition, since Xfoil does not calculate flow fields, no comparisons of circulations or bubble height could be made.[27]

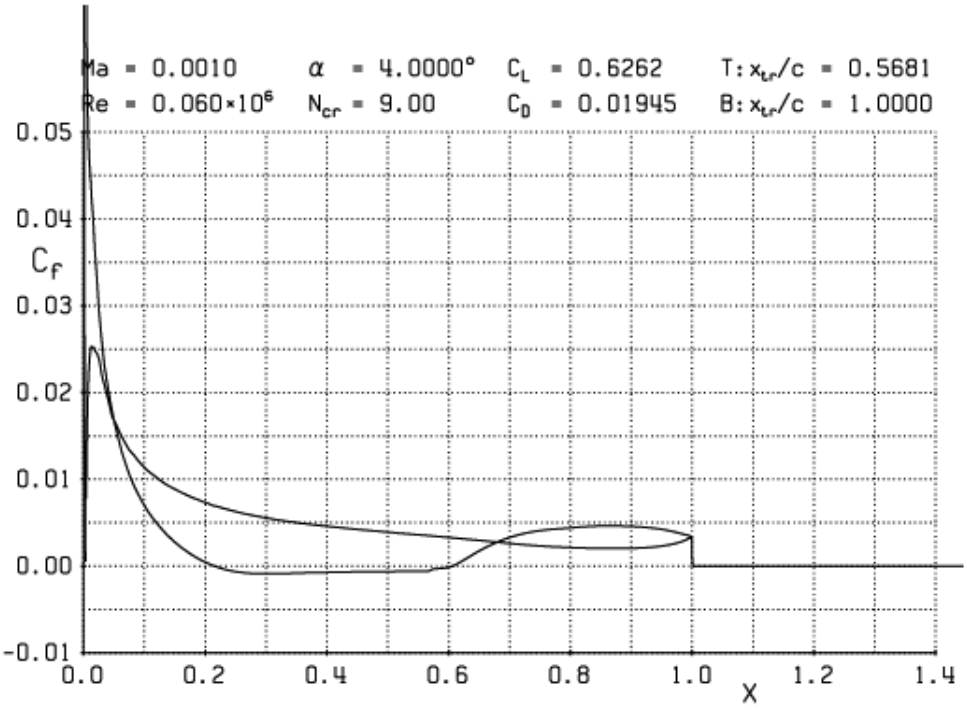

Figure 1.11: The laminar separation bubble for the SD7003 airfoil (Ol)
A plot of skin friction coeffient vs chord-wise location for the SD7003 at Re $= 6 \times 10^4$ and $\alpha = 4°$. This result is from Xfoil using a critical N-value of 9. The location of the LSB is indicated by the region where the skin friction coefficient is negative. [27]

In a study by Mohseni et al, the computation of the flow field around an aspect ratio 1.2 flying-wing airplane at Re $= 1.4 \times 10^5$ using an E387 airfoil was also able to calculate the presence of an LSB. [14] The 3-dimensional computation used a direct numeric simulation of the Navier-Stokes equations, and makes no mention of any transition or turbulence models. At this Re, it is unclear whether the computation they describe has the spatial and temporal resolution to capture the transition to turbulence. There is no comparison to measurements made on a similar configuration, but they did compare computed force on a flat plate at various α to measurements made by Mueller et al. As shown in figure 1.12, the computational results were not in good agreement with the

measurements. This questions the validity of the computational technique, and the LSB computed by it. Furthermore, the Re of this computation is well above that shown to be the Re that causes the drag increase at moderate lift coefficients.

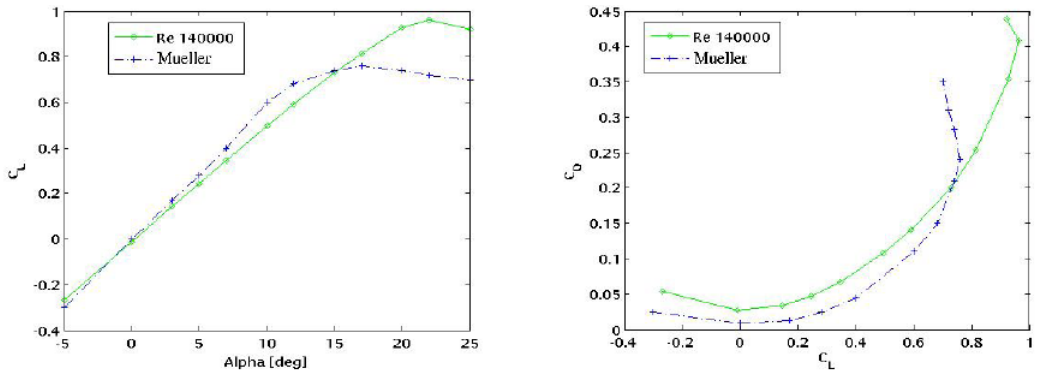

Figure 1.12: Lift and drag of a flat plate airfoil (Mohseni)
The forces from computational results of Mohseni et al are compared to the experimental measurements of Mueller et al for a flat plate at Re $= 1.4 \times 10^5$. The disagreement here is substantial, with the maximum lift being more than 20% greater and the minimum drag being more than 50% greater than the experimental measurements. [14]

Finally, in a study by Radespiel et al, a computational technique based on linear stability theory of boundary layers was used to compute the LSB on a SD7003 airfoil at Re $= 6 \times 10^4$, $\alpha = 4°$,8°,11° , and in both steady and unsteady flow. The computational technique is similar to Xfoil in that it computes the external flow, the boundary-layer profile, and relies on a critical N-value to identify the location of transition to turbulence. The difference is that it uses an Unsteady Reynolds-Averaged Navier-Stokes (URANS) equation to compute the external and boundary layer flow rather than the panel-method and boundary layer equations used by Xfoil. Once the critical N-value has been reached, the URANS equation computes both the spatial and temporal growth of the turbulence from the point of transition, which is required for unsteady computations.

The computational results are compared to experimental measurements taken at the same conditions. The experimental measurements consisted of PIV measurements which resolved the boundary layer flow, and hence visualized the LSB. An example of the experiments and computations are shown in figure 1.13 where the experiments are labeled as WUB, and the rest are computational results with various turbulence models. The turbulence level in the experiments was 0.8%, 8 times as large as the turbulence level that effects the transition of a flat plate boundary layer. It is unclear whether computations should be compared with experimental results that have such large values of free-stream turbulence.

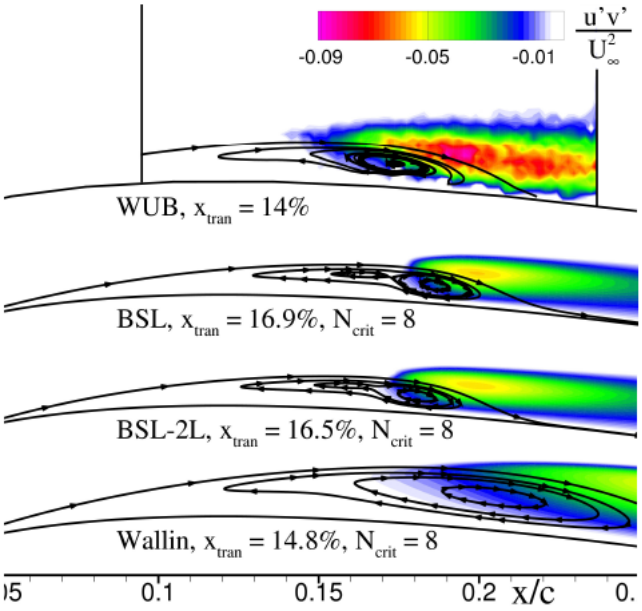

Figure 1.13: The laminar separation bubble on the SD7003 airfoil (Radespiel) Experimental and computational results at Re $= 6 \times 10^4$ and $\alpha = 8°$. The WUB result is from PIV measurements in a water channel, and the other three are from computations with various turbulence models. Streamlines are indicated by lines with arrows, and turbulent shear is indicated by the color map. The transition point is listed in percentage of the chord, and the critical N-value is 8 for this comparison. [30]

Streamlines are plotted along with the normalized turbulent shear, an indication of the turbulence intensity. The LSB can be seen as the region of recirculating flow, and the transition to turbulence seems to be caused by the shear layer of the LSB. The plots are for $\alpha = 8^\circ$ and three types of turbulence models are used in the computations. The first two are developed by Menter and are called the baseline (BSL) and the baseline 2-layer (BSL-2L) models. The third is from Wallin and can be used for both compressible and incompressible turbulent boundary layers. For this application, it seems that the BSL models perform the best, and based on comparisons at other α and using various other critical N-values, Readespiel et al determine that the BSL-2L model is the most appropriate, although they point out that the computations are not completely satisfactory.

In addition to comparing the LSB computations to experimental measurements of the LSB, they also compared the forces computed to forces measured by Selig et al in [35] [36]. The comparison in figure 1.14 shows the lift coefficient plotted against α and the drag coefficient. The open symbols are plotted against α and the filled symbols are plotted against the drag coefficient. Despite the large differences in computed LSB size and shape, the forces computed by each of the turbulence models are quite similar and all are within the experiments conducted by Selig et al. Granted the experiments were conducted more than 5 years apart and at two different wind tunnel facilities, but this comparison seems to indicate that while an LSB exists for this airfoil at this Re and α, it does not seem to significantly affect the forces generated by the airfoil. This plot also indicates that a basic understanding of which drag polar is correct limits one's ability to validate a computational technique.

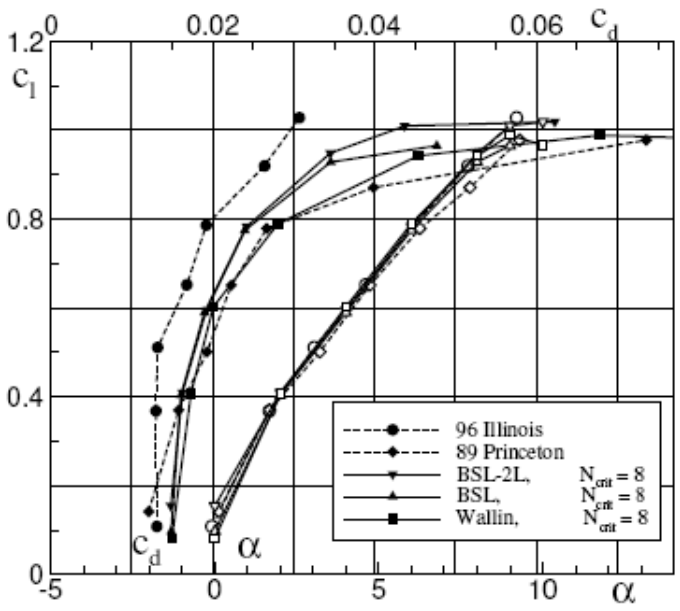

Figure 1.14: Drag polar for SD7003 airfoil. (Radespiel)
The experimentally measured results from Illinois and Princeton (dashed lines) are compared to the computational results of Radespiel et al (solid lines). The lift coefficient vs α is shown in the filled symbols while the open circles are lift coefficient vs drag coefficient. The airfoil is at Re$= 6 \times 10^4$. [30]

1.5 Leading Edge Vortex

Another type of laminar separation followed by reattachment to the airfoil surface is a leading edge vortex (LEV). This LEV is formed by separation at the sharp leading edge of a wing during the downstroke of the flapping cycle. The separation rolls up on top of the wing, and forms a vortex near the leading edge. The flow outside the vortex is able to reattach to the airfoil surface. The reason for the roll up of the separation is the stabilizing effects of span-wise flow from the wing center to the wing tip. This span-wise flow causes the vortex to form a helical shape as it travels down the span.

Many studies on biological flying systems (especially insects) have revealed that a dominant feature of the flow physics of a flapping wing at low Re is the formation of an LEV. [20] [10] [39] [9] This LEV can be described using the Weis-Fogh effect, where

insects “clap” their wings together above their bodies, then “fling” them apart. This is the so called clap-fling mechanism of insect flight.

More recently, there have been studies that have measured an LEV on the fixed, swept wing of a Swift, a small bird. [40] [19] The first study at $3.7 \times 10^3 < \text{Re} < 3.7 \times 10^4$ indicated that the 60° swept hand-wing of the Swift develops an LEV at an angle of attack of $\alpha = 10^\circ$ and it was speculated that the LEV may cause an increase in lift. [40] The study was performed on the frozen wing of a Swift placed in a wind tunnel, and it was noted that the wing was able to passively flex and rotate in the wind. The feathers of the wing were smoothed down, and a force balance was used to measure the forces. Flow field measurements were made near the wing to identify the formation of the LEV.

However, the later study shows that the LEV appears only at $\alpha > 30^\circ$ and does not provide an increase in lift. [19] The wing for this study was manufactured in a machine shop, however it was also able to flex and rotate passively. The sweep of the wing was varied by rotating the wings back, thus changing the aspect ratio and area of the wing. Force balance measurements were made in a wind tunnel, and flow field measurements were made to identify the presence of an LEV. The two results are contradictory, and no resolution has been found thus far.

Chapter 2

Problem Statement

2.1 Force Measurements

There is a very limited amount of data on the forces generated by airfoils and wings at $10^4 <$ Re $< 10^5$. There was only one study mentioned in the previous chapter [18] that was focused solely on this range of Re, and this was also the only study of airfoils and wings at Re $< 5 \times 10^4$. Every other study was typically focused on Re $> 10^5$.

Since planes are currently being built with operational Re as low as 3×10^4, and since there is much interest in operating at even smaller Re, it is important to understand how the forces generated change throughout the entire range of $10^4 <$ Re $< 10^5$.

Measuring forces at these low Re is a challenge because the forces are so small. Since the lift is typically an order of magnitude larger than the drag, lift measurements have typically been done using a strain gauge force balance. However, drag measurements have often relied on the wake defect. Due to the span-wise variation in the wake of wings at these low Re, this technique can yield inaccurate results.

Some studies that have attempted to measure drag at these low Re using a force balance with a minimum resolvable force that is near the drag forces measured. The only reliable measurements of both the lift and the drag of airfoils and wings at this Re was employed by Laitone in his use of a strain gauge force balance that was capable of resolving very small forces (0.1 mN). [18]

2.2 Eppler 387 Performance

The E387 is one of the most widely studied airfoils at Re $\approx 10^5$. The previous chapter showed reliable force measurements made at various facilities. The measurements were in relatively good agreement when Re $\geq 10^5$, but at Re $= 6 \times 10^4$ (the lowest Re of the studies) there was considerable disagreement in the measurements. Also, at this Re, there was a drastic drag increase at moderate lift coefficients.

The source of these discrepancies is not fully understood, and the cause of this drag increase has not been identified satisfactorily. Further, it is not clear what happens to the forces as the Re decreases below 6×10^4.

2.3 Model Geometries

Any flying vehicle will have a finite aspect ratio. Thus far, the majority of the tests have restricted themselves to studies of 2D airfoil geometries by using end plates. If the goal is to gather data useful the flying vehicles, then some study should be done of finite aspect ratio wings to understand how aspect ratio effects the aerodynamics of wings at this range of Re.

Studying both finite aspect ratio wings and 2D airfoils allows comparisons to be made using potential flow theories like Thin Airfoil Theory and Lifting Line Theory. Comparisons have been made before (by Laitone [18] and Mueller [29]), with contradictory results. It is still unclear whether these theories apply at Re $< 10^5$.

2.4 Laminar Separation Bubble

The laminar separation bubble is currently used to explain the peculiar drag increase at moderate lift coefficients often seen for airfoils at low Re (eg. the E387 at Re $= 6 \times 10^4$).

Selig calls this drag increase the bubble drag. However, experiments done thus far to measure the LSB have focused on cases where there is very little bubble drag. The results of Selig [38] and Broeren and Bragg [8] showed surface oil flow visualization for the E387 at Re $> 2 \times 10^5$. However, at these Re, the E387 has no drag increase at moderate lift coefficients (see figure 1.4). The bubble drag doesn't seem to be present until Re $< 1 \times 10^5$. When an experiment to visualize the LSB was performed at Re $< 1 \times 10^5$, it was performed on the SD7003 airfoil that has no drag increase at moderate lift coefficients (see figure 1.10). [27] [36]

Furthermore, every study of the LSB has been conducted at a small number of angles of attack and Re, and none have studied how the forces generated by the wing are affected by the presence or absence of the LSB. There is no study of the both the forces generated by and airfoil and its boundary layer when it has a drag increase at moderate lift coefficients.

2.5 Leading Edge Vortex

Previous measurements of the LEV formed on swept wings at Re $< 10^5$ have been conducted from a biological perspective: to identify fluid-dynamic mechanisms that explain how a specific bird flies. However, when building new small scale flying devices, this is not as useful as taking an engineering perspective: to identify the important parameters that cause these fluid-dynamic mechanisms to form. Previous experiments have been done on model bird wings that have taper, non-constant airfoil geometry, non-constant sweep angle, and feathers. They also have some amount of flexibility that allows them to flex and rotate, giving an undefined dihedral angle and α. Furthermore, when they study the effect of sweep, they often vary the aspect ratio, stream-wise chord length, and area of the wing as well.

Chapter 3

Proposal

There has been very little research on the forces produced by wings and airfoils at Re $< 10^5$. Of the research that has been done, the large majority has been conducted with inadequate techniques (e.g. using the wake deficit to estimate the drag coefficient), and only one reliable study has been conducted at Re $< 6 \times 10^4$ (the study by Laitone).

The first objective of this study is to measure the forces produced by some wings and airfoils at Re $< 6 \times 10^4$. This "survey study" will provide information on the forces produced by various airfoil shapes. The measurements will be made for 3 airfoil shapes, at 2 Re, in 2D and 3D conditions, and at a large range of α.

Force measurements have been made by many facilities on the E387 airfoil, using endplates, at Re $= 6 \times 10^4$, and they have consistently found a drag increase at moderate lift coefficients that is not seen at higher Re for this airfoil, but is a common feature of other airfoils at this Re. While the measurements are in agreement as to the existence of a drag increase at moderate lift coefficients, there is relatively large disagreements about the exact size and extent of the drag increase. There has yet to be any study of the forces generated by this airfoil at Re $< 6 \times 10^4$ to help explain either the drag increase, or the disagreement in the data.

The second objective of this study is to determine what happens to the lift and drag produced by the E387 airfoil as the Re is decreased below 6×10^4. End plates will be used to provide comparisons to previous data, but measurements will also be made for a 3-dimensional geometry to determine if the drag increase at moderate lift coefficients is particular to 2D geometries.

It is currently thought that this drag increase is caused by the formation of a Laminar Separation Bubble (LSB), however there has been limited data to support this conclusion. Currently, surface oil flow visualizations of the E387 have shown the existence of an LSB, but only at Re $> 10^5$ where there is no drag increase at moderate lift coefficients. There have also been flow field measurements that resolve the LSB of the SD7003 airfoil at Re $= 6 \times 10^4$, but this airfoil shows no drag increase at moderate lift coefficients at this Re.

Thus, the third objective of this study is to show conclusive evidence of whether or not the LSB is causing the drag increase experienced by the E387 airfoil at Re $= 6 \times 10^4$. By taking flow field measurements that can resolve the LSB at a range of Re and α, this will be the first study to document the formation, growth and breakdown of the LSB. The quantitative measurements of the boundary layer flow field can be compared to computational results to test the validity of current computational models and techniques.

Another laminar separation followed by reattachment has been identified and is often called the leading edge vortex (LEV). This LEV has been identified for flapping wings at low Re, however recent experiments show that a LEV may be formed by swept, thin, cambered wings at low Re as well. The conclusion of two experiments are contradictory at this point, and neither experiment has conducted a controlled study where a single parameter is varied.

This is the fourth objective of the study: to show the effect of sweep on the formation of an LEV at low Re. By keeping all other parameters constant and only changing the sweep of a thin, cambered wing, the effect of sweep on the LEV formation will be found. Detailed measurements of the LEV using quantitative flow field measurements will provide more information on how the LEV forms. Finally, force measurements of

the swept wing will prove whether or not the LEV provides increased lift for a simple cambered wing.

3.1 Force Measurements

Force measurements will be made for 3 airfoil geometries: a flat plate, a cambered plate, and the E387 airfoil. The flat plate airfoil will have a 5:1 elliptical leading edge, followed by a constant 2.5% thick section, and the final 17% of the chord will be a linear taper to the trailing edge. The cambered plate will be identical to the flat plate, except that the entire airfoil will be curved to have a circular camber line with maximum camber of 5% located at the mid-chord. The E387 is defined as a third order spline through the points provided by reference [35]. The flat plate is chosen to allow comparison to analytical models such as the drag on a flat plate calculated from a Blasius boundary layer. The cambered plate is chosen to allow comparison to Laitone who studied a 5% cambered airfoil at Re $= 2 \times 10^4$. The E387 is a high performance sail plane airfoil that has been studied by many facilities at Re $= 6 \times 10^4$.

These three airfoil shapes will be studied at Re $= 1 \times 10^4$ and 2×10^4 across a range of $-10^\circ < \alpha < 20^\circ$ in 1° increments. The wings will have 3.5 cm chord, an aspect ratio of 6, and will be milled from aluminum using a CNC mill to ensure precision of geometry. The wings will be lightly sanded and painted to ensure a smooth surface. The 2D airfoil performance will be measured by using end plates located within 1 mm of the wing tips. This is compared to an estimated boundary layer thickness of 1.6 mm at the trailing edge of the wings at the lowest Re.

3.2 Eppler 387 Performance

Additional force measurements will be made for the E387 airfoil at $3 \times 10^4 <$ Re $< 6 \times 10^4$ in 10^4. A larger wing with a 9 cm chord will be machined for these higher Re measurements. The large and the small E387 wing will be tested at the same Re to ensure similar results from both models.

These additional measurements will show how the forces generated by the E387 change as Re decreases below 6×10^4. The measurements at the highest Re will also allow comparison to previous studies.

3.3 Laminar Separation Bubble

Flow field measurements will be made to resolve the LSB on the upper surface of the E387 airfoil at Re $= 6 \times 10^4$. The LSB measurements will be made for select α but will include the regions of α both before and after the drag increase at moderate lift coefficients.

From this data, a detailed understanding of how the LSB effects the forces generated by the E387 wing at these Re will be obtained. Up to this point, there has been no systematic test across α that measures both the forces and the boundary layer flow. This study will provide the evidence to show exactly when and how the LSB grows and decays across a range of α.

3.4 Leading Edge Vortex

There has been no study of a simple wing, where the only design parameter that is varied is the sweep. All studies that have been done have included non-zero taper and other complicating factors. They also have variations in aspect ratio and other important

parameters while measuring the LEV. This study will determine the effect of sweep on the LEV formed over simple cambered wings at these low Re. The results should explain the conditions under which an LEV forms, and they will help guide further, more detailed studies of swept wings at low Re.

Initial dye visualization experiments will be conducted in a water channel to identify the sweep angles and α of interest in forming an LEV. Simple, constant chord, constant sweep, thin, cambered wing will be used. Quantitative flow field measurements will be made in the wind tunnel on a model that forms an LEV, and force measurements will be made to identify how the LEV effects the forces generated by a simple swept wing.

Chapter 4

Methods

4.1 Wind Tunnel

The Dryden Wind Tunnel will be used for this study. It is a closed wind tunnel with 12 anti-turbulence screens, and the ratio of the settling chamber cross sectional area to the test section cross sectional area is 7:1. The test section (shown in figure 4.1) is octagonal, and the parallel edges are 1.37 m apart, which gives a cross sectional area of 1.56 m^2. The test section has three transparent windows, located on top, on the side, and on the lower left hand corner.

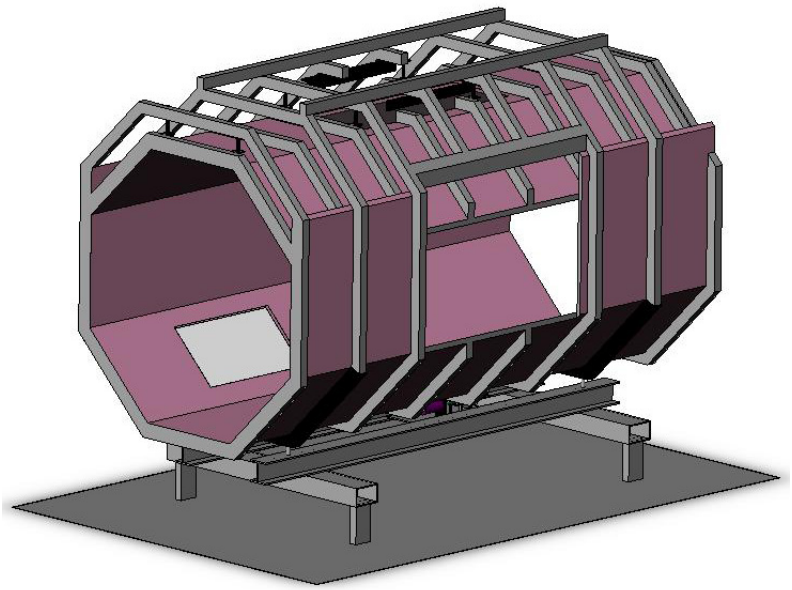

Figure 4.1: The USC Dryden Wind Tunnel Test Section
A 3D view of the USC Dryden Wind Tunnel test section. The three viewing windows are on the top, the side, and at the bottom left.

The relatively large number of anti-turbulence screens and the relatively large contraction ratio provides very low turbulence intensities in the free-stream of the test section. The turbulence intensity is defined as

$$q = 100 \times \frac{u'}{U} \tag{4.1}$$

Much care was taken in measuring the turbulence in the test section because at Re $< 10^5$, it can have a large effect on the measurements made. The turbulence measurements were made with a hot-wire anemometer probe. Measurements were made across the test section area to ensure spatial homogeneity.

The hot-wire apparatus consists of a 1.5 μm tungsten wire attached to a support. The wire is supplied with a voltage from an A. A. Laboratory Systems hot wire signal conditioning unit. The current running through the wire increases the temperature of the wire. Since the resistance of the wire is directly related to the temperature, this increase in temperature will increase the resistance. When the hot-wire is placed in a flow, the temperature of the wire is decreased proportional to the velocity of the flow. The signal conditioning unit adjusts the voltage to maintain a constant wire resistance, and hence a constant temperature of the wire. If there is higher velocity, then less voltage and current will be required to maintain a constant resistance and temperature of the wire. Thus, the voltage required is inversely related to the velocity of the flow. The thermoelectric properties of the wire, and the small diameter, result in frequency responses up to 1 kHz. This high frequency response allows the measurement of the rapid fluctuations referred to as free-stream turbulence.

Results of the turbulence measurement show that the turbulence level is uniform across the test section, and is always below 0.03%. A measurement of the velocity fluctuations was done in the upper right quadrant of the wind tunnel, and figure 4.2 is a plot of the RMS of the velocity fluctuations plotted across that section of the wind

tunnel. The average turbulence in the wind tunnel is 0.025%, which is well below the 0.1% identified by Schubauer and Skramstad [33] as causing early transition on flat plates. Thus, the effect of turbulence on the present tests should be minimal.

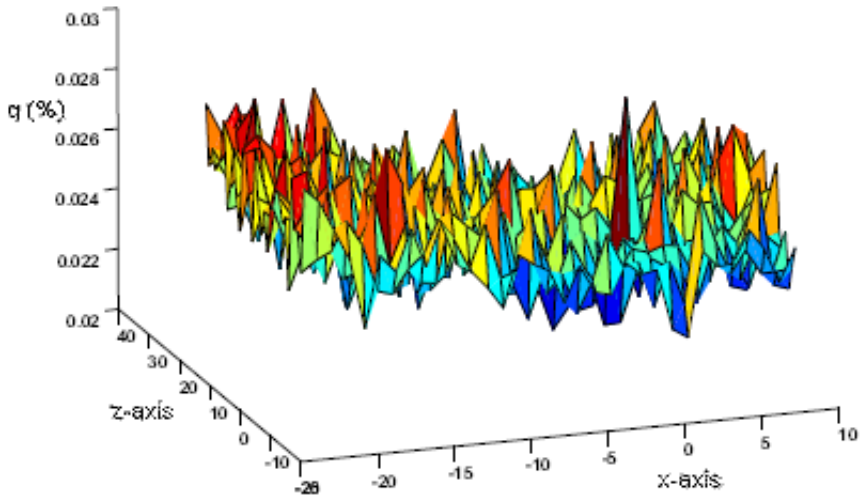

Figure 4.2: Wind Tunnel Turbulence Uniformity
A plot of RMS velocity fluctuations in the USC Dryden Wind Tunnel. The x-axis is the location in the horizontal cross-stream direction, while the z-axis is the vertical cross-stream direction. The ordinate is the turbulence intensity at a given point in the wind tunnel. The plot is for the upper right corner of the wind tunnel, and the center of the wind tunnel is at (0,0).

4.2 Force Balance

For measuring forces in the wind tunnel, a custom-made force balance will be used. The force balance resembles a 3 layer sandwich composed of a bottom plate, a cruciform in the middle, and a top plate. The bottom plate attaches to the cruciform at two opposing endpoints of the cruciform, while the top plate attaches at the other two opposing endpoints. In figure 4.3 the long side-arms on the left and right attach to the top plate. Four strain gauges are located on each arm of the crucifix, and they form a wheatstone bridge

which is used to measure the deflection of each arm. The strain at each strain gauge location is maximized for a given deflection by hollowing out the arm, and placing the strain gauge at the thinnest point of the arm.

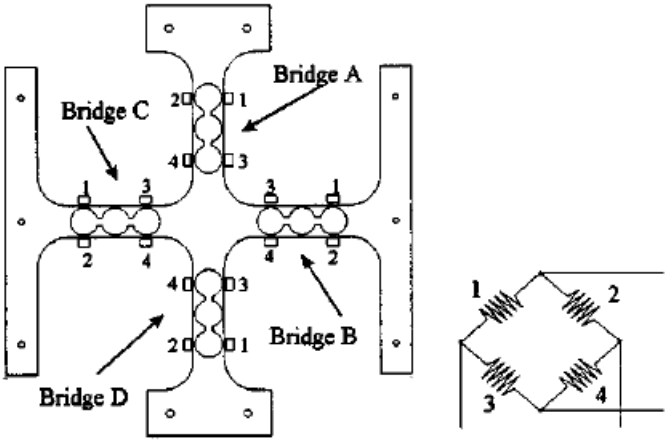

Figure 4.3: Force Balance Planform
The long side arms attach to the top plate, while the short side arms attach to the bottom plate. Four strain gauges are placed at the thinnest points of each arm, and as far from each other as possible. These form a wheatstone bridge: the excitation voltage is applied from top-to-bottom, and the bridge voltage is measured across the left and right corners.

In the diagram, the output voltage of bridge A and D are sensitive to horizontal forces, while bridge B and C are sensitive to vertical forces. Thus, any force applied to the force balance can be resolved into two directions which are decoupled and measured independently. Combining the voltages from the bridges (V_A, V_B, V_C, V_D), one can produce 2 voltages related to the forces.

$$V_{Horizontal} = V_A + V_D$$

$$V_{Vertical} = V_B + V_C$$

Any out-of-plane moment applied to the force balance will not effect the output of these 2 voltages. This is because of the symmetry in the design. A calibration between the forces applied to the force balance and the voltages recorded, yields the calibration coefficients. For improved accuracy of the measurements, a cross-talk calibration scheme is employed which allows both forces to each effect the voltages described above. The following equation describes the cross-talk:

$$V_{Horizontal} = A_{11}F_{Horizontal} + A_{12}F_{Vertical} + A_{13}$$

$$V_{Vertical} = A_{21}F_{Horizontal} + A_{22}F_{Vertical} + A_{23}$$

where A is the calibration matrix, and F is the forces applied in the given direction. Cross-talk is important because it has been observed that applying a horizontal force causes a small but significant affect on the vertical voltage, and vice-versa. When running an experiment, this set of equations must be inverted to yield the forces as a function of the voltages measured:

$$F_{Horizontal} = B_{11}V_{Horizontal} + B_{12}V_{Vertical} + B_{13}$$

$$F_{Vertical} = B_{21}V_{Horizontal} + B_{22}V_{Vertical} + B_{23}$$

where B is now the calibration matrix.

To measure the small forces of the wings at low Re with a force balance, the small voltages produced by the force balance must be measured. An estimate of the magnitude of the lift and drag forces of a wing can be made using the standard equations:

$$L = C_L\frac{1}{2}\rho \mathrm{U}^2 \mathrm{cb}$$

$$D = C_D\frac{1}{2}\rho \mathrm{U}^2 \mathrm{cb}$$

where C_L and C_D, are the lift and drag coefficients respectively, and c and b are the chord and the span of the wing respectively. Rearranging these equations in terms of the Re, and the aspect ratio (A) yields:

$$L = C_L \frac{1}{2} \frac{\mu^2}{\rho} \mathrm{Re}^2 \mathrm{A}$$

$$D = C_D \frac{1}{2} \frac{\mu^2}{\rho} \mathrm{Re}^2 \mathrm{A}$$

From this set of equations, one can take any previous experiments and calculate the magnitude of the forces and moments by only knowing the fluid properties, the Re, and the aspect ratio. Referring to figure 1.4, the C_L and C_D will likely range from 0 to 1.5 and from 0.01 to 0.1 respectively. From these estimates of the coefficients, assuming normal atmospheric conditions for μ and ρ, working at a the lowest Re of this study (1×10^4), and an aspect ratio 6 wing with 3.5 cm chord, the lift and drag forces will vary from 0 to 100 mN and from 0.8 mN to 8 mN.

The force balance is connected to a signal processing board that applies the excitation voltage and amplifies the bridge output voltage. At the largest amplification factor available, the force balance has a nominal sensitivity of 1 $\frac{\mathrm{mV}}{\mathrm{mN}}$. This amplified bridge voltage is sent to a computer via a 12-bit analog-to-digital (ADC) converter with 10 volt range. This gives a 2.5 mV resolution of the ADC, which is not adequate for measuring the drag forces at this Re. However, the electronic noise in the system is set above the resolution, and can be used to enhance the resolution by over-sampling and averaging the measurement.[17] The effective number of bits (ENOB) is calculated with the oversampling ratio (OR):

$$\mathrm{ENOB} = \mathrm{NOB} + \log_4(\mathrm{OR})$$

where the 4 is a constant of the equation, and the NOB is the number of bits of the ADC. For this study, 8000 samples were made over the course of 8 seconds and averaged to provide one measurement of the forces. Thus, the oversampling ratio was 8000. This provides an ENOB of 18.5, and a minimum resolvable voltage of 0.05 mV. This is sufficient to resolve the minimum drag force at this Re.

Repeated calibrations showed that the relationship between voltages and forces was linear and consistent over multiple measurements. The calibrations were performed using objects that were measured on a commercial scale with resolution of 0.01 mN, and the calibration was performed in the wind tunnel to minimize any disturbances due to location or moving the force balance. The force balance was placed under the wind tunnel, and a steel rod (commonly referred to as the "sting") was connected to it. The sting protrudes into the wind tunnel, and the wings were designed to be placed at the end of the sting, in the center of the wind tunnel. The calibration was performed by pulling on the end of the sting in the lift and drag directions. Objects were placed in cups with a string attached that wrapped around a pulley and connected to the sting.

An example of the calibration results for the drag at Re $= 1 \times 10^4$ is shown in figure 4.4. This plot is generated after each calibration to ensure it was done correctly. The abscissa is the drag forces used during the calibration while the ordinate is the drag forces predicted by using the measured voltages and the calibration coefficient. For a perfect calibration, the points would be in a straight line with a slope of 1. A linear curve fit is plotted along with the calibration points and the equation and R-squared value is shown. The slope is within 0.1% of 1, as is the R-squared value, which is sufficient for this study. Uncertainty is estimated by the RMS of the difference between predicted and actual forces at each calibration point. The uncertainty is estimated to be 0.0003 mN for the drag calibration shown above, and error bars are plotted but are smaller than the symbol size.

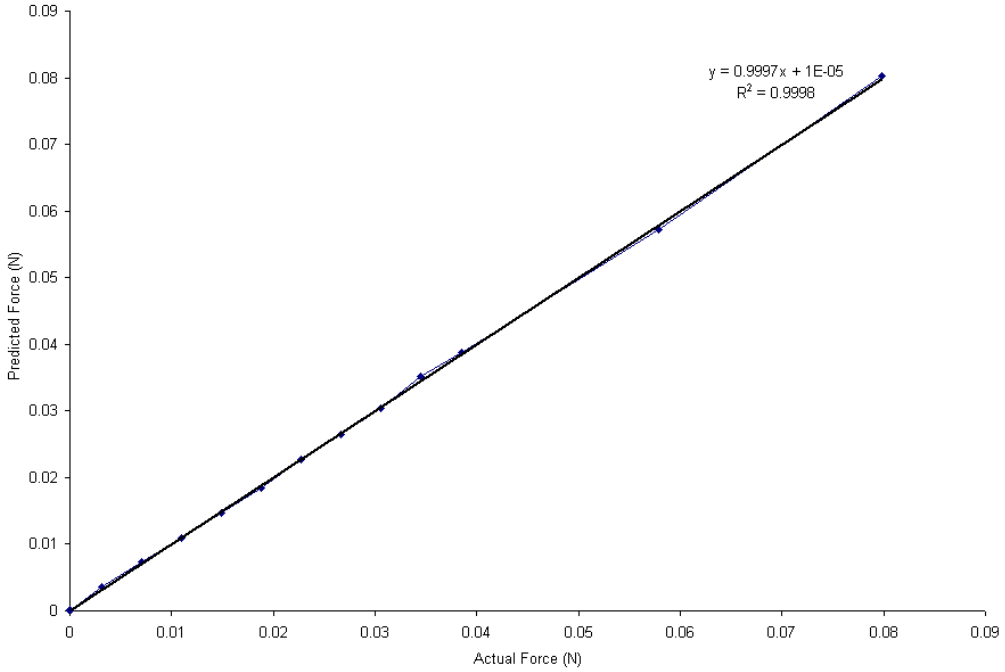

Figure 4.4: Drag Calibration Results
Calibration of the Drag for the lowest Re measurements. The abscissa is the actual force applied in the drag direction, while the ordinate is the force calculated using the measured voltages and the calibration coefficients. Error bars to represent the uncertainty are smaller than the symbol size.

The calibration weights used may seem too large based on the estimate of the forces given earlier. The drag for the current experiments was estimated to vary between 0.8 mN and 8 mN at Re $= 1 \times 10^4$. The calibration only contains two calibration points below 10 mN, which is not sufficient. However, the drag estimate was based on drag coefficient measurements made by Selig et al at Re $= 6 \times 10^4$. As Re decreases below this Re, the drag coefficient increases dramatically, and experience has shown the actual drag at Re $= 1 \times 10^4$ varies between 5 mN and 30 mN. Thus, the current calibrations are sufficient for the measurements made.

4.3 Particle Image Velocimetry

For the flow visualization, a custom made Particle Image Velocimetry (PIV) system will be employed. A PIV system works by seeding a flow with particles that act as passive tracers of the velocity field. Two images are taken of the particles in rapid succession in such a manner that the majority of the particles in the first image are still present in the second image. Then, particle displacements are computed by comparing the two images. Dividing the particle displacements by the time between the images yields the instantaneous velocity at each point. For the current experiment, a laser is used to illuminate a single plane of the flow and thus only 2 components of the velocity field can be measured. The PIV algorithm used to calculate the velocity field in this experiment is called Correlation Image Velocimetry (CIV) and has been documented previously in [11]. All image velocimetry algorithms are focused on the correct reconstruction of both the velocity fields and the spatial gradients, regardless of computational cost.

A Kodak ES 1.0 CCD camera with 1008 x 1018 pixels will be placed above the wind tunnel to capture images. It is connected to a frame grabber card on a digital computer to acquire the images. Two lenses will be used for the study. The first has a focal length of 85 mm and can visualize approximately a 12 cm x 12 cm region at the center of the wind tunnel. This is large enough to capture the flow field around the larger E387 wing with a chord of 9 cm. The other lens has a focal length range of 80-200 mm and can focus on a region as small as 1.8 cm x 1.8 cm at the center of the wind tunnel. This lens will be primarily used to visualize the boundary layer of the larger E387 wing and identify separation and reattachment points.

The wind tunnel flow will be seeded with smoke particles generated by heating oil past its boiling point using a Colt 4 smoke generator. The smoke particles have a nominal diameter of 3 μm and act as passive tracers of the velocity field. Two lasers will be used to illuminate a sheet of particles in the wind tunnel. The lasers are 6 W Nd-Yag lasers

with 4 ns nominal pulse-width and a repetition rate of 10 Hz. The lasers are fired in rapid succession (typically about 100 μs) and are timed with a Stanford timing box capable of 1 ns pulse separation. The amount of time between the two lasers firing is determined by the velocity in the wind tunnel and the zoom of the camera. The objective is to have an average particle displacement that is approximately 5 pixels. Thus, the time between pulses is

$$\Delta t = \frac{5}{\mathrm{UZ}}$$

where Δt is the time between pulses, the 5 is for the 5 pixel displacement, and Z is the pixels/cm of the camera.

The beam of the lasers is converted to a sheet by using a series of cylindrical and spherical lenses. The objective is to have a wide, thin sheet with adequate amounts to energy to illuminate the particles. The first lens is a spherical lens which acts to focus the beam. The next lens is a cylindrical-diverging lens which acts to stretch the beam and create a sheet. The final lens is another cylindrical-diverging lens, but oriented perpendicular to the previous lens. It straightens the sheet edges and creates a nearly constant thickness sheet in the beam direction.

The PIV correlation algorithm works by allowing the user to select the size of the correlation and search boxes in number of pixels. The process is to take a correlation box in the first image, and search (within the search box size) for the highest correlation in the second image. The algorithm can achieve sub-pixel resolution by plotting the correlation value for each point in the search box, then curve fitting a smoothed spline surface to it and selecting the location where the curve fit is maximized. This technique has been verified for various cases, and yields a velocity bandwidth of approximately 1/200, which means that velocities are accurate to about 0.5% of the maximum value measured. [11]

Calibration of the PIV system was performed by printing crosses onto a sheet of paper, placing the paper at the location of the laser sheet, focusing the camera on the paper, and taking a picture. The pixels per cm was calculated by image analysis of this reference target. A typical resolution of the camera with the 80 mm lens was 84.4 ± 0.2 pixels/cm.

In any PIV experiment, data acquisition parameters and algorithm settings must be adjusted appropriately for flow complexity. In the present experiments, the sheet thickness was approximately 1 mm thick at the center, and approximately 20 cm wide across the wing tunnel. The timing between images was adjusted based on the ability of the CIV algorithm to find good correlations. Time between images was nominally 200 μs. For the CIV algorithm, a correlation box size of 30 pixels, and the search box size of 44 pixels was typically used.

Chapter 5

Results

5.1 Force Measurements

Force measurements have been made for the flat plate, cambered plate, and E387 airfoils. The measurements were made at Re $= 1 \times 10^4$ and 2×10^4 for the range $-10^\circ < \alpha < 20^\circ$ in 1° increments. Tests have been run with and without end plates to measure 2D airfoil performance, as well as aspect ratio 6 wing performance. The first comparison is of each airfoil shape, at both Re, for the 2D and 3D cases. The measurements for Re $= 1 \times 10^4$ at 2D and 3D conditions are shown in figures 5.1(a) and 5.1(b) respectively, while figures 5.2(a) and 5.2(b) are measurements for Re $= 2 \times 10^4$ at 2D and 3D conditions, respectively. To save time, the flat plate was not measured at all $\alpha < 0$ because it is symmetric. For each plot, the lift and drag coefficients are plotted versus α and error bars indicate the standard deviation of 4 measurements. For each measurement, the wing was started at the lowest α, then increased to the highest, then decreased back to the lowest. This was done to check for hysteresis.

The cambered plate airfoil attains higher lift coefficients than the E387 airfoil, which has lift coefficients that are often less than the flat plate. This is true for the 2D and 3D cases. In fact, the flat plate attains a higher maximum lift-to-drag ratio than the E387 at Re $= 1 \times 10^4$. This is shown in figure 5.3. Since lift-to-drag ratio is a common measure of efficiency for an airfoil, the flat plate would be more efficient than a specially designed airfoil. This is true even considering the measurement uncertainty, which is relatively large because of the relatively large uncertainty in the drag coefficient.

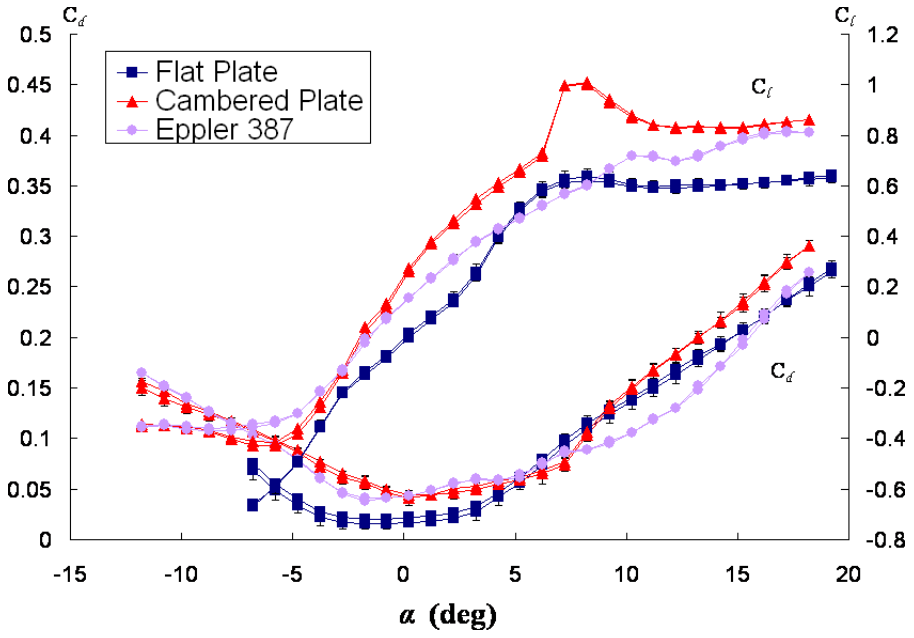

(a) With Endplates - 2D airfoil

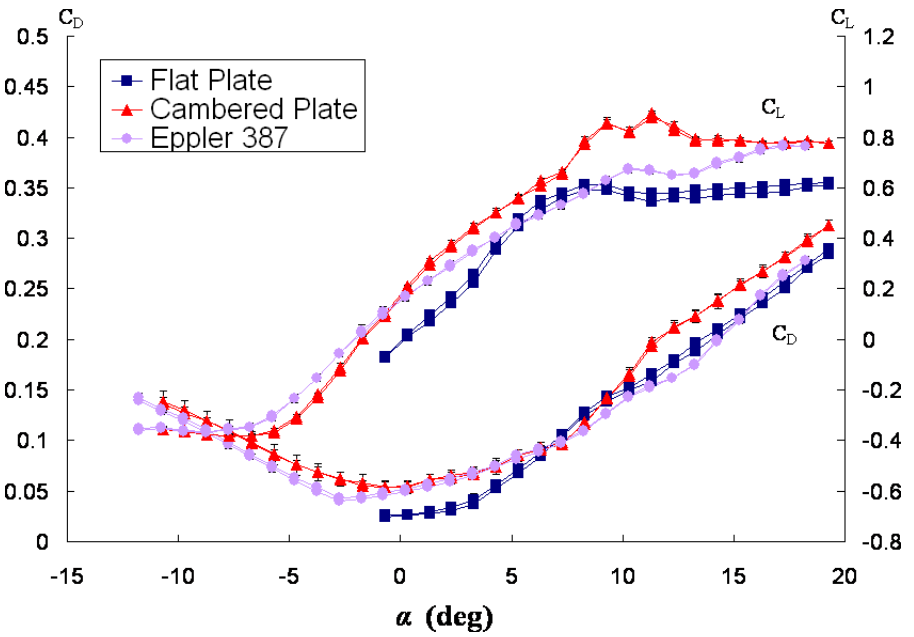

(b) Without Endplates - Aspect Ratio 6 wing

Figure 5.1: Airfoil force coefficients at Re $= 1 \times 10^4$

The force coefficients for each airfoil at Re $= 1 \times 10^4$. Increasing and decreasing α are plotted, and error bars represent standard deviations of 4 independent measurements. Error bars are much smaller than the symbol size for the lift measurements, but are visible for the drag measurements.

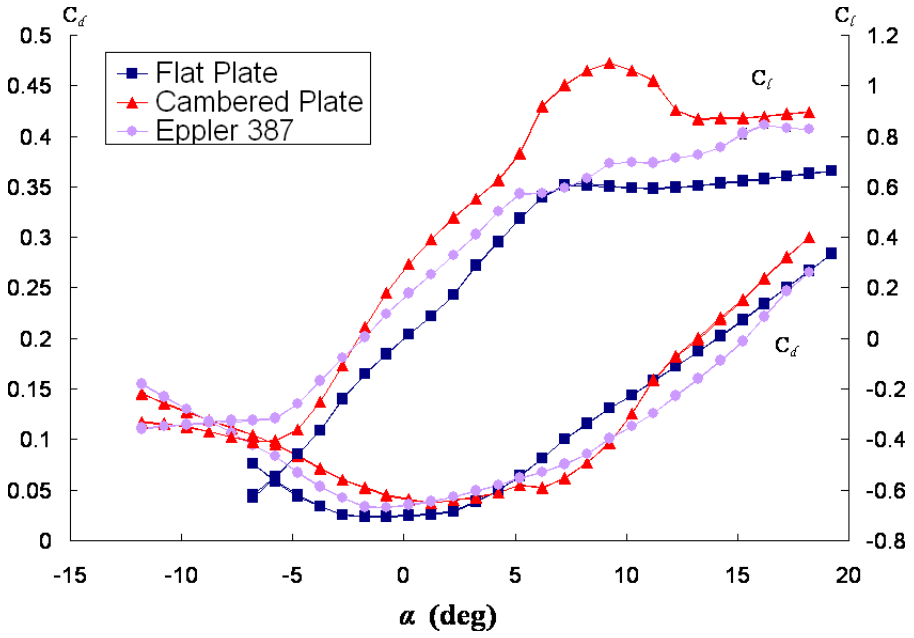

(a) With Endplates - 2D airfoil

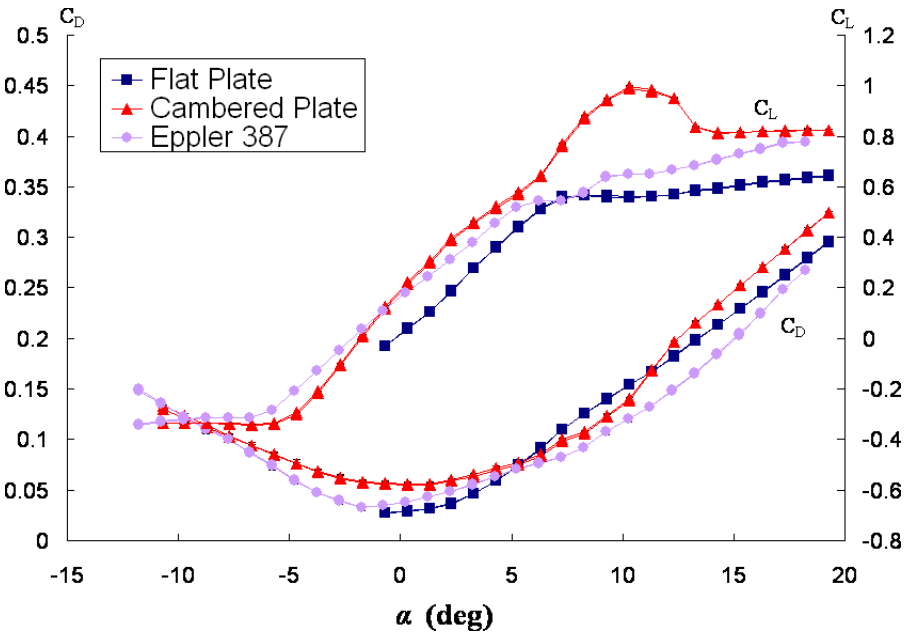

(b) Without Endplates - Aspect Ratio 6 wing

Figure 5.2: Airfoil force coefficients at Re $= 2 \times 10^4$

The force coefficients for each airfoil at Re $= 2 \times 10^4$. Data acquisition and uncertainty estimate techniques are similar to those in figure 5.1 but error bars are covered by the symbols for both the lift and the drag data.

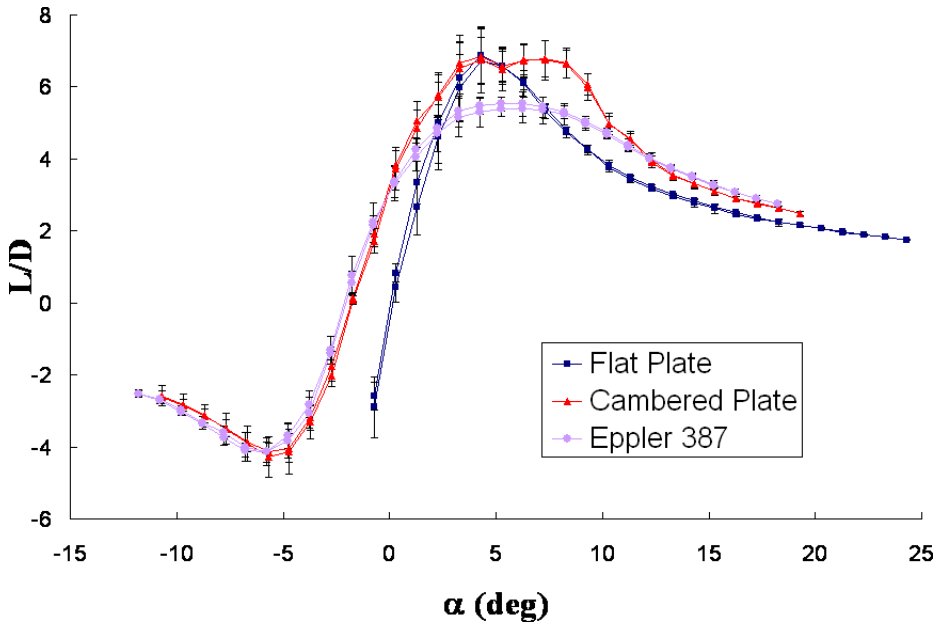

Figure 5.3: Lift-to-drag ratio at Re $= 1 \times 10^4$
This plot is for the 3D case where end plates are not used. The flat plate clearly has a larger lift-to-drag ratio than the specially designed E387 airfoil, even when considering the uncertainty. The flat plate also attains a higher lift-to-drag ratio in 2D conditions.

5.2 Eppler 387 Performance

Lift and drag measurements have been made for the E387 airfoil at Re = 1, 2, 3, and 6×10^4. The measurements were made at $-10^\circ < \alpha < 20^\circ$ in 1° increments. The lowest two Re were obtained with the smaller wing (3.5 cm chord), while the highest two Re were obtained with the larger wing (9 cm chord). Plots of lift and drag coefficient vs α are shown in figure 5.4(a). For this data, end plates were used to approximate 2D flow conditions. Figure 5.4(b) shows the force coefficients for the aspect ratio 6 case. In both plots, hysteresis was investigated by making measurements while increasing and decreasing α. The uncertainty was estimated by running 4 experiments and taking the standard deviation. Error bars are plotted in the figures, but they are smaller than the

symbol size. Plots of the lift-to-drag ratio for the above cases is shown in figure 5.5(a) and 5.5(b).

Both the 2D and the aspect ratio 6 data show the sudden lift increase, and drag decrease experienced by the E387 at Re $= 6 \times 10^4$. As the Re decreases to 3×10^4, the magnitude of the drag decrease goes down, and at Re $= 2 \times 10^4$ the drag is monotonic with α. The lift-to-drag ratio shows a gradual progression as Re increases. The maximum lift-to-drag ratio increases rapidly with Re, consistent with the generalization of McMasters (see figure 1.2). [24]

The drag polar for this airfoil is plotted in figure 5.6 at the 4 Re studied. Both the 2D and the aspect ratio 6 cases are plotted for comparison. In figure 5.7, the 2D case is plotted with previous studies of the E387 at Re $= 6 \times 10^4$ (see figure 1.4). The current measurements are qualitatively similar to previous measurements, with the characteristic drag increase at moderate lift coefficients. At high lift coefficients (larger than 1), there is a difference between the current measurements and previous measurements. The previous experiments measure a larger lift increase and drag decrease compared to the current measurements. One possible explanation for this difference is that the previous experiments all use the wake deficit technique to estimate the drag. Another possible explanation is that all previous experiments had turbulence intensities greater than the current tests, and many were above the 0.1% limit for a flat plate.

The most recent of the previous measurements shown in figure 5.7 was taken as part of a larger study at the University of Illinois Urbana Champagne (UIUC). As part of that study, force measurements at larger Re were also taken (see figure 1.4). The current measurements are plotted and compared with this data in figure 5.8. This plot indicates a clear range in which the polar of the E387 changes drastically. According to Selig, the drag increase at moderate lift coefficients seen at Re $= 6 \times 10^4$ is caused by a large laminar separation bubble (LSB), and the subsequent drag decrease at higher

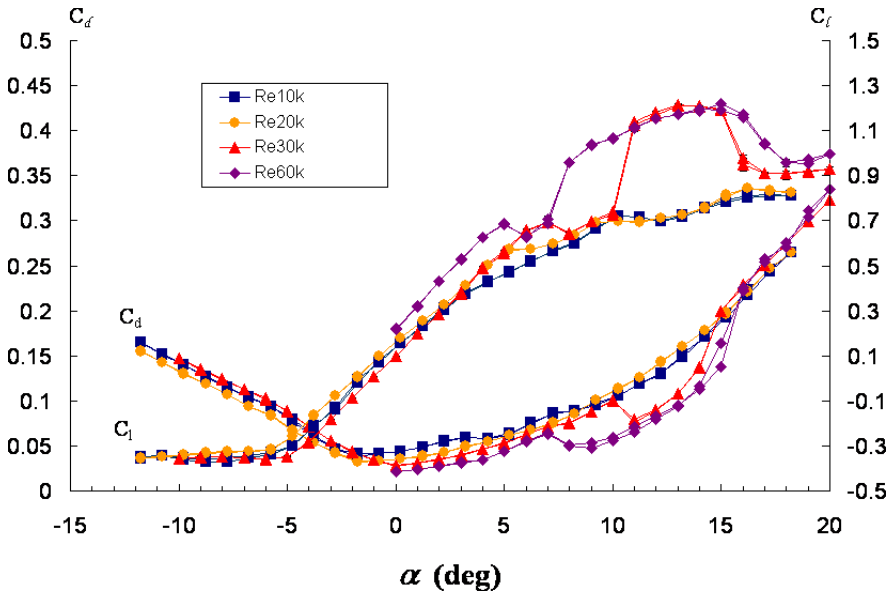

(a) With Endplates - 2D airfoil

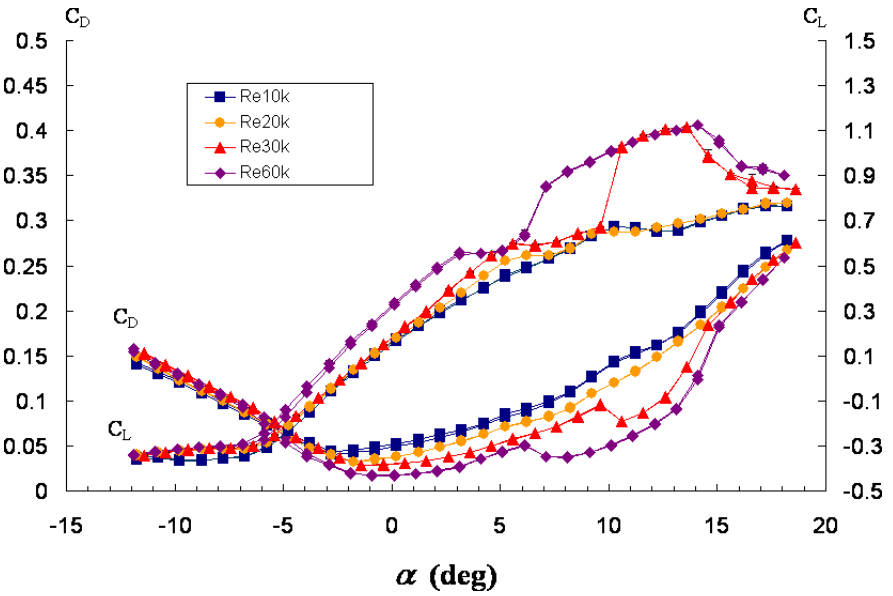

(b) Without Endplates - Aspect Ratio 6 wing

Figure 5.4: Eppler 387 Performance Curves
The lift and drag coefficient vs α for the E387 airfoil. Data was taken for both increasing and decreasing α. The uncertainty is plotted with error bars, but is smaller than the symbols.

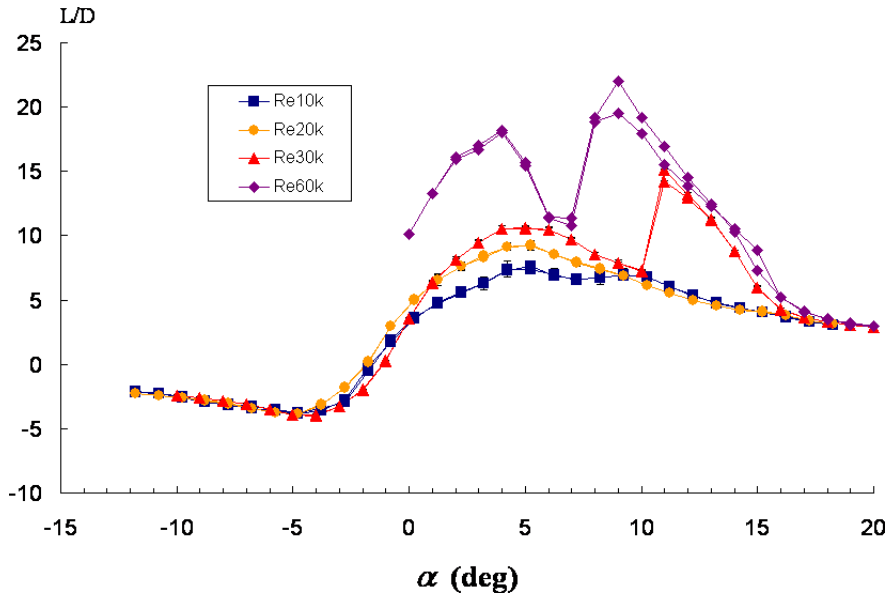

(a) With Endplates - 2D airfoil

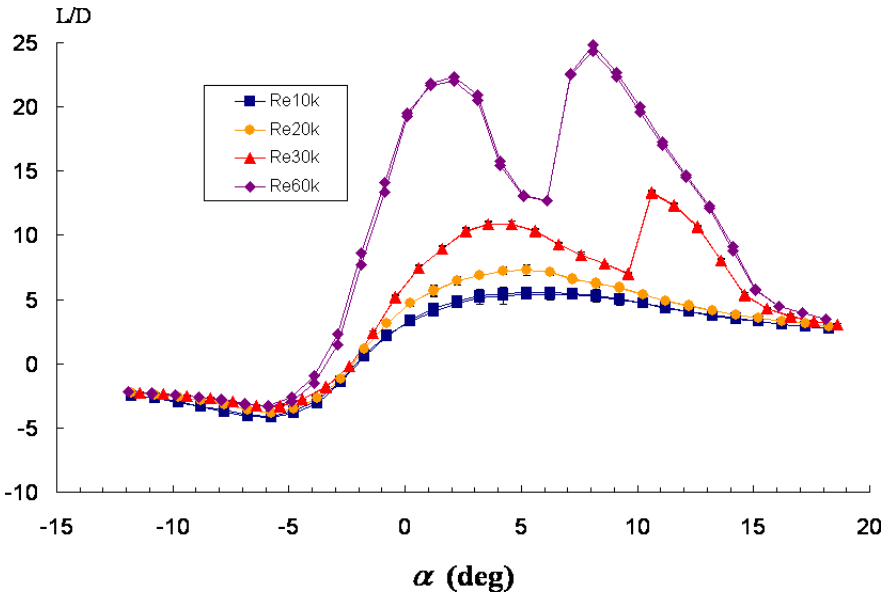

(b) Without Endplates - Aspect Ratio 6 wing

Figure 5.5: Eppler 387 Lift-to-Drag Ratio
The lift-to-drag ratio of the data plotted in figure 5.4. Uncertainty estimates are plotted with error bars, but are typically covered by the symbols.

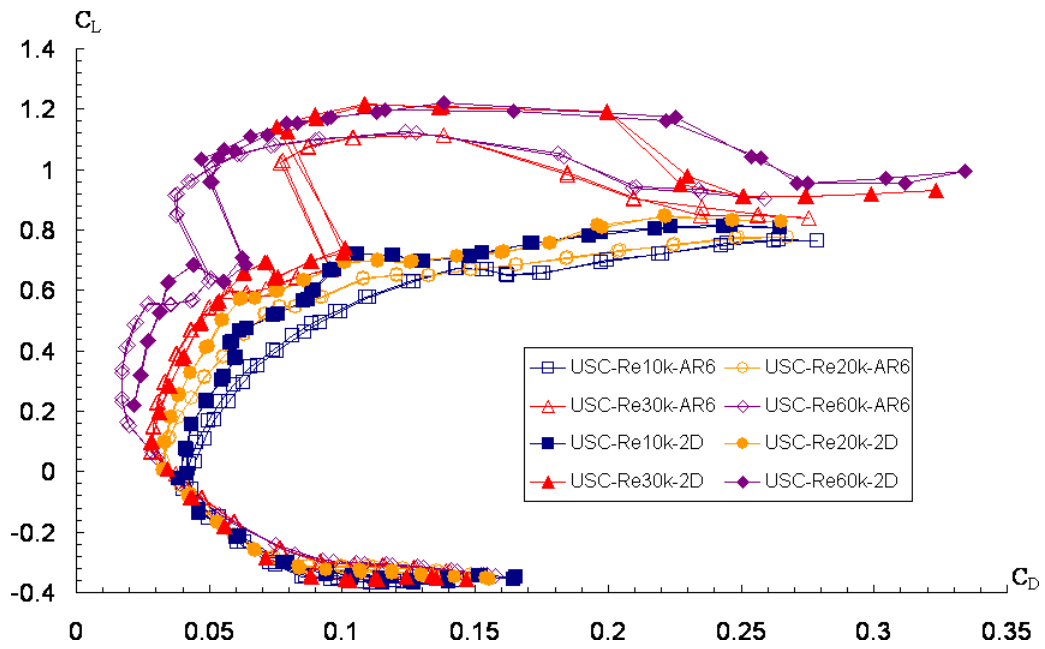

Figure 5.6: Eppler 387 Drag Polars - 2D and 3D cases
The drag polar for the E387 at 4 diffent Re, and both 2D and aspect ratio 6.

α is caused by the bubble bursting and becoming very small. However, there is rather limited evidence for this conclusion, and in light of the present measurements at much lower Re, a new possible interpretation is offered. *The drag increase at moderate lift coefficients is caused by simple laminar separation with no transition to turbulence and no reattachment. The subsequent drag decrease at higher α is caused by the formation of an LSB.*

This new interpretation can be understood by considering the relatively rapid drag increase at the lower Re, as compared to the higher Re. Since the boundary layer at Re $= 1 \times 10^4$ is laminar and does not transition to turbulence before reaching the trailing edge, this rapid drag increase is most likely caused by the laminar separation point moving up the chord as α increases. At Re $= 6 \times 10^4$, the lower α have a similarly rapid drag increase. This suggests that the drag increase at moderate lift coefficients is likely caused by laminar boundary layer separation with no reattachment. However, when the

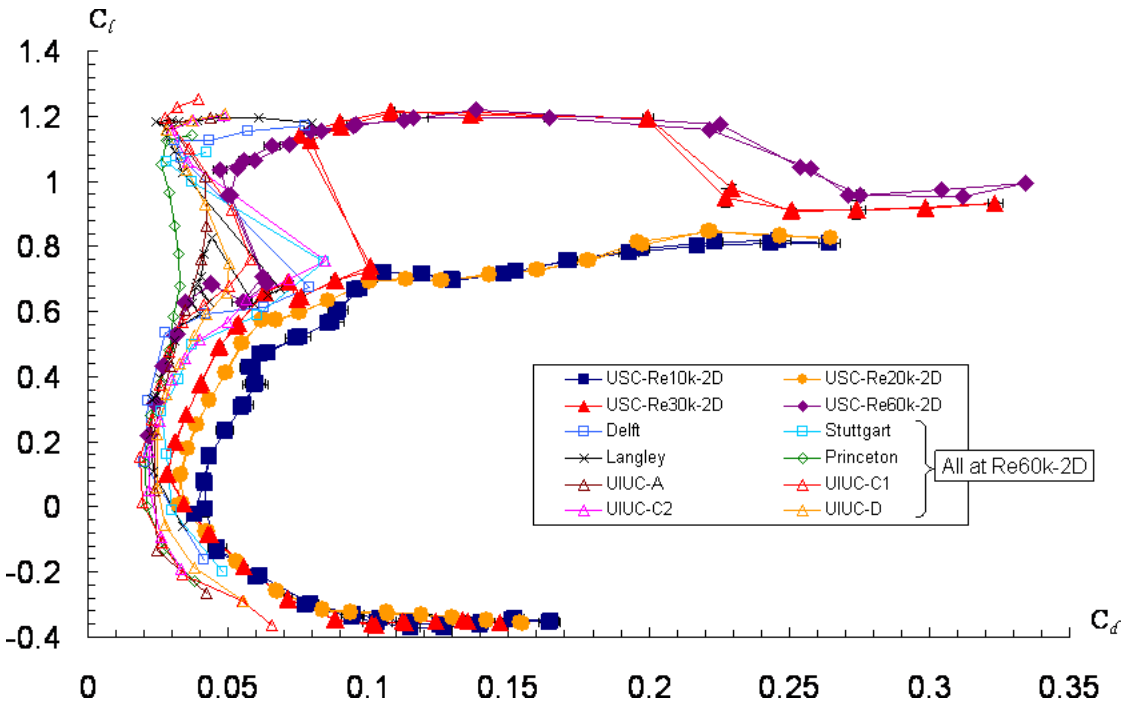

Figure 5.7: Eppler 387 Drag Polars - 2D Comparisons - 60k
Comparison of the current experiments to previous experiments conducted at various facilities. All previous measurements shown here were conducted at Re $= 6 \times 10^4$ and in 2D conditions.

drag suddenly decreases and the lift increases, there must be a change in the flow. This is the α when the LSB forms, and by reattaching to the upper surface the lift is greatly increased and the drag is decreased.

One way of understanding why the LSB forms at this particular Re is by considering the length of the chord. At Re $= 1 \times 10^4$, there will be a laminar free-shear layer directly downstream of the separation point. Free-shear layers are known to be more unstable, and can transition to turbulence more quickly than a boundary layer. However, at these low Re, the shear layer does not transition before reaching the end of the airfoil, and hence there is no reattachment. Since the Re is proportional to the chord when assuming density, speed and viscosity to be constant, then as Re increases, there is more distance (and hence time) for the shear layer to transition before reaching the end of the

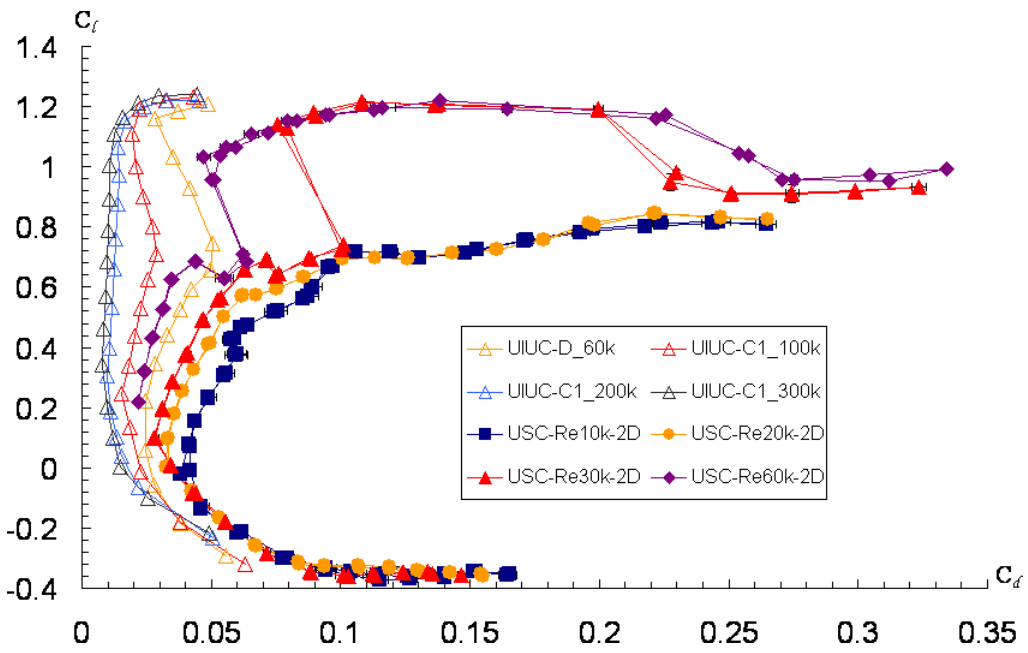

Figure 5.8: Eppler 387 Drag Polars - 2D Comparisons - UIUC
The most recent measurements of the E387 airfoil done by UIUC at a range of Re. The current measurements compare well, and show that this is the critical Re range for the airfoil.

airfoil. Thus, as Re increases, the laminar shear layer is capable of transitioning and reattaching to the airfoil.

There are 2 possible explanations for why the LSB forms at particular α. The first is similar to the explanation above: since the laminar separation point moves forward as α increases, then there will be more distance for the shear layer to transition at higher α. The second explanation is that the instability of the shear layer depends on the shape of the shear layer velocity profile, and on the shear layer Re. As α increases, the changes in the shear layer velocity profile and shear layer Re will increase the instability. With larger instability, the shear layer will transition more rapidly and will reattach to the airfoil in a shorter distance.

5.3 Flow Field Measurements

The flow field around and behind the E387 airfoil has been measured at Re $= 1 \times 10^4$ and 2×10^4 with the PIV system described in chapter 4. The 85 mm lens (12 cm-by-12 cm viewing area) and the smaller wing (3.5 cm chord) were used. A raw image pair for Re $= 1 \times 10^4$ and $\alpha = 10^\circ$ is shown in figure 5.9. The flow is from left to right. The laser illuminates from the top of the image, and hits the upper surface of the airfoil. The glare at the surface is caused by diffuse reflection of the laser sheet, and measurements in the glare region are impossible. The shadow cast by the wing is seen as the dark region below the wing. Since this data was not capable of resolving the boundary layer of the wing, the purpose of showing these results is as an example of the PIV process and results.

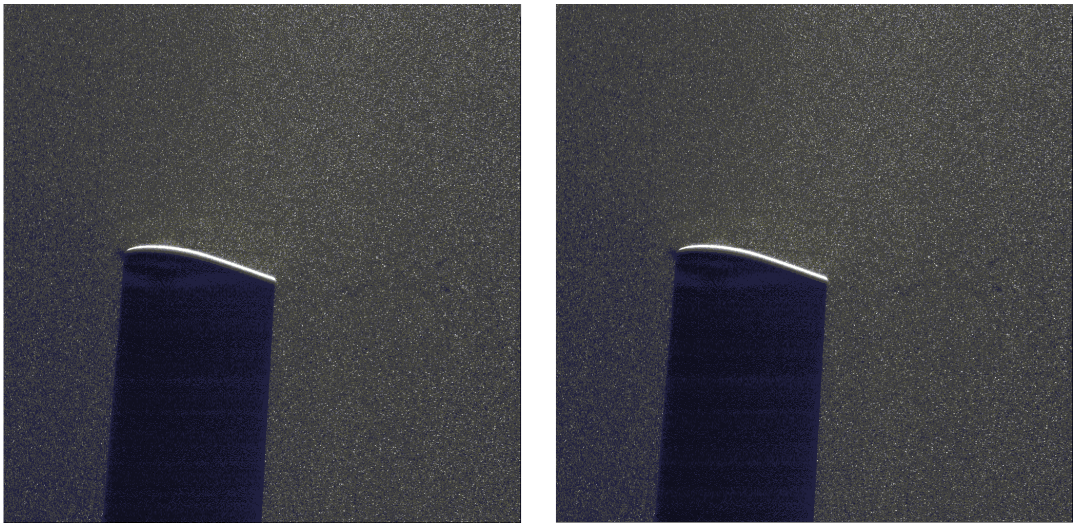

Figure 5.9: PIV results - Raw Image Pair
A raw image pair taken 160 μs apart. The images have been scaled down to 25% of their original size, so it is difficult to see the particles. The glare on the upper surface makes velocity measurements near the surface impossible. To avoid that problem in the future experiments, the wing will be highly polished.

The second image was taken 160 μs after the first image, and the average particle displacement is approximately 5 pixels. The PIV correlation algorithm uses this image pair to find particle displacements. The flow field for the above image pair is shown in figure 5.10. The free stream flow can be seen above the wing, near the top of the figure, while to the right of the figure is the wake, seen in the oscillatory nature of the flow. The flow field is in the lab reference frame, with the air flowing past the wing. To switch to the LaGrangian reference frame, the free-stream mean flow must be subtracted from each velocity vector. The upper portion of the flow is chosen as the free stream, and an average velocity vector is computed. This is removed from every velocity vector in the field. The result is shown in figure 5.11. This shows the displacement velocity field, and the wake is clearly visible. Also, the outer flow acceleration over the upper surface is visible.

By taking the gradient of the velocity field at every point, the vorticity of the flow field can be found. For a 2D flow field, the spanwise vorticity is:

$$\omega_y = \frac{\partial w}{\partial x} - \frac{\partial u}{\partial z}$$

where x is the stream-wise direction, y is the span-wise direction perpendicular to x, z is the direction perpendicular to both of them, and (u, v, w) are the components of the velocity vector in the (x, y, z) directions. The vorticity map of the above case is shown in figure 5.12. The wake of the wing is seen as the characteristic vortex street, with a wave length and frequency. Vorticity is also contained on the wing, near the trailing edge.

This PIV technique, with a higher magnification lens, will be capable of resolving the boundary layer separation and reattachment at the higher Re cases where a larger wing will be used. To avoid problems with the glare from the upper surface, the wing

will be polished to a mirror finish to minimize diffuse reflections. This should keep the laser sheet in a single plane, and allow for visualization near the surface.

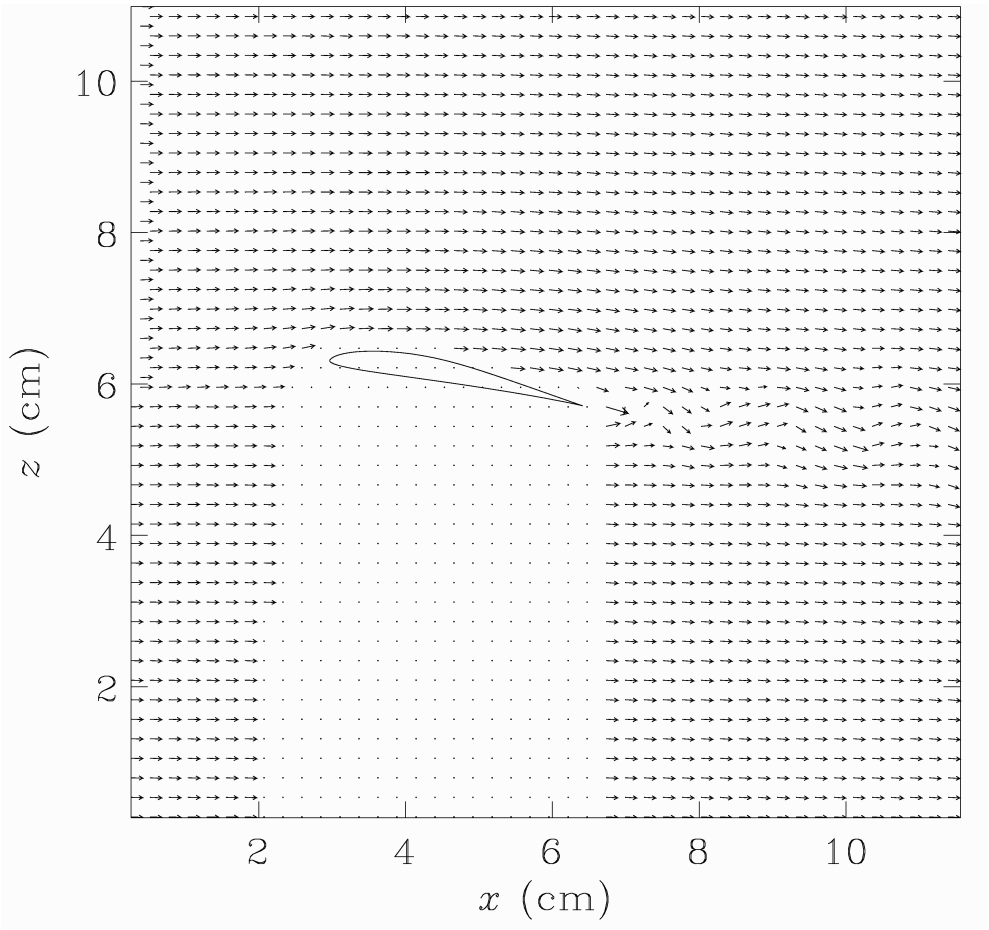

Figure 5.10: Example Flow Field with Mean Flow
The velocity field for the E387 airfoil at Re =1×10^4 and $\alpha = 10°$. This is taken at the mid-wing of the airfoil, and there are no end-plates used. For clarity, the velocity vectors are doubled in length, and the spatial resolution is halved.

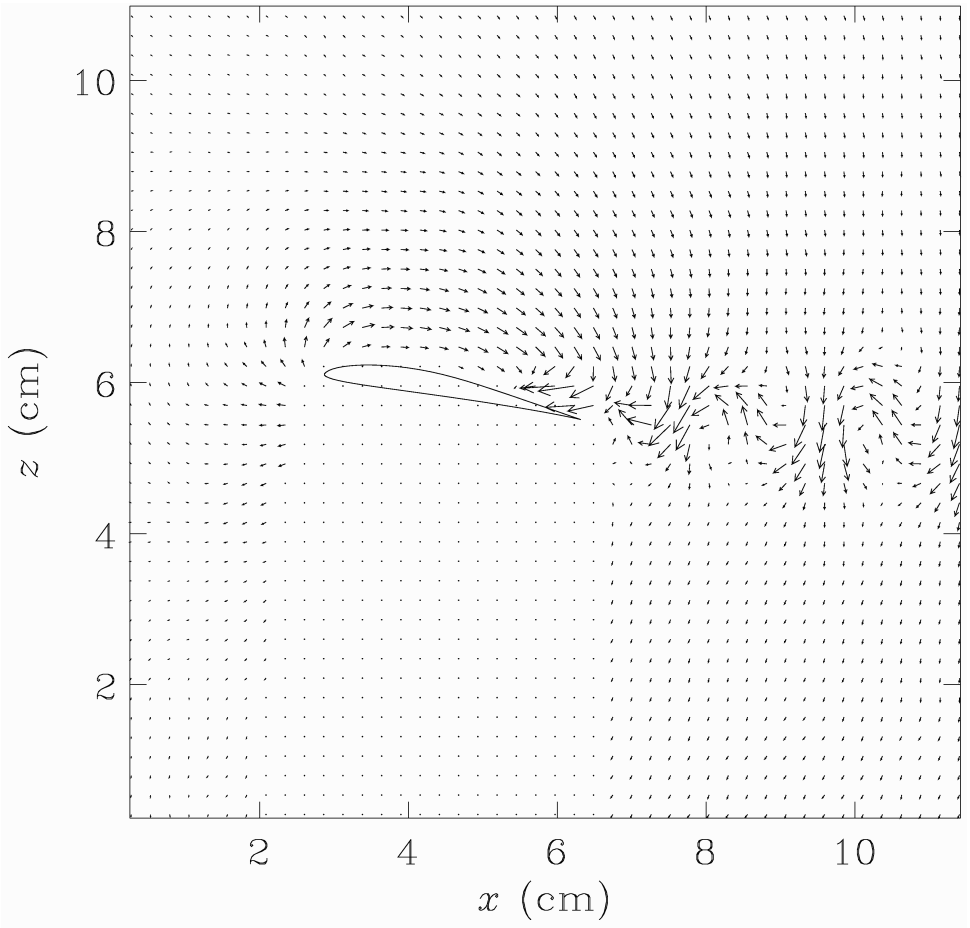

Figure 5.11: Example Flow Field with no Mean Flow
The velocity vector field of figure 5.10 with the free-stream flow removed. The free-stream flow was calculated as the average flow in the upper-left corner. In this frame of reference, the wing can be thought of as moving through a quiescent fluid. The velocity vectors here are plotted at 10 times there actual length.

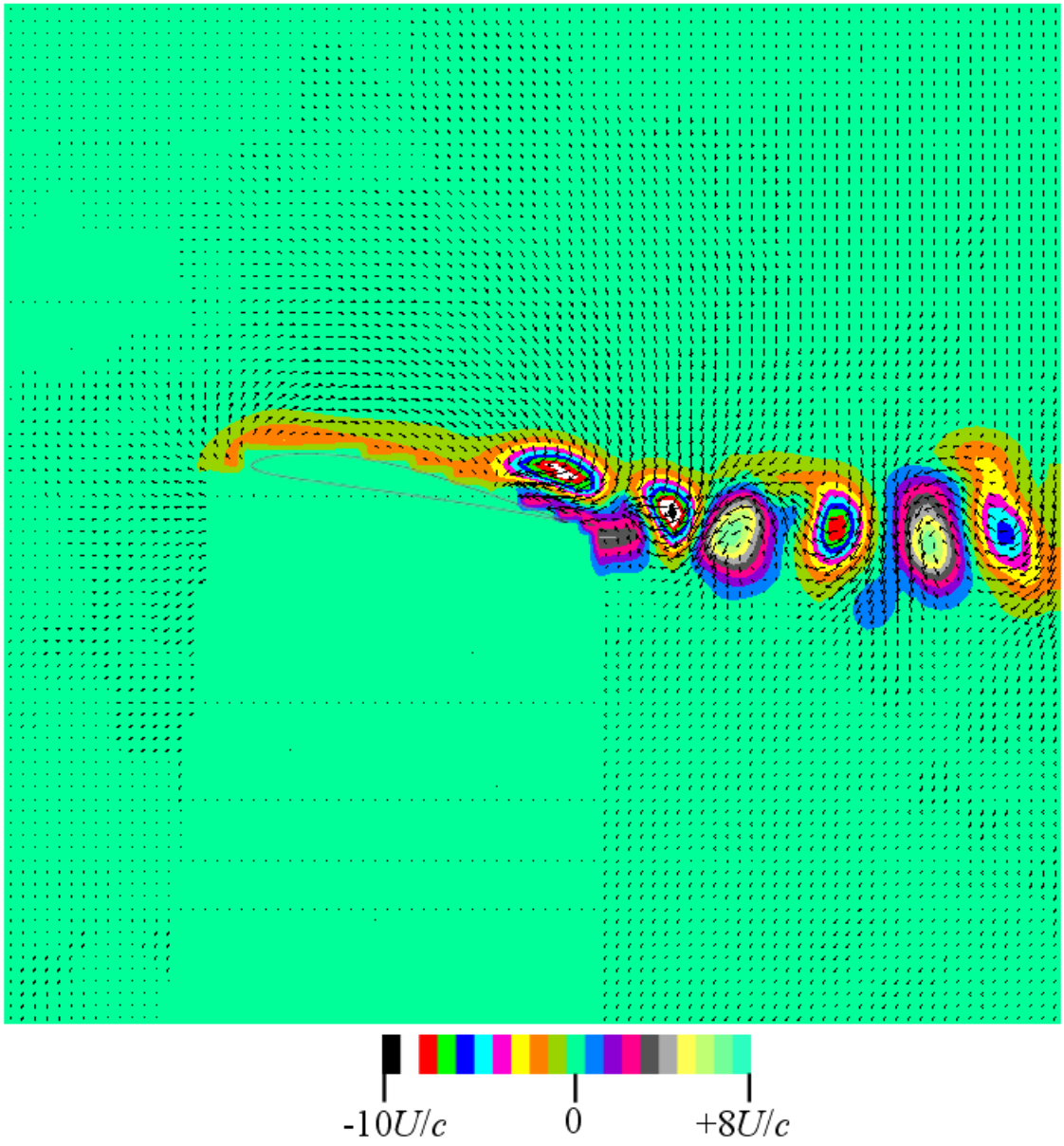

Figure 5.12: Example Vorticity Map

The vorticity contours of figure 5.11. The color bar is shown, and has been normalized by the convective frequency. The vector lengths are now 6 times there real length, and the resolution is the real resolution of the experiment.

5.4 Leading Edge Vortex

Flow visualization experiments using dye injection were performed for a swept wings. Experiments were conducted in a water channel, and pictures and videos were taken to document the flow around the swept wings. The goal was to identify sweep angles and α where a LEV is able to form.

Four wings were made of 0.08 cm thick brass shim stock, each with a 4.45 cm chord, 5% circular-arc cambered airfoil and sweep angles: 0, 20, 40, 60°. Each wing has an aspect ratio of 6, an area of 119 cm^2, a thickness ratio of 1.8% (0.08/4.45), and no taper. The wings were made by rolling the shim stock to the specified camber, then soldering each half of the wing together. The sting (support mount) was made by stacking 3 pieces of the same brass shim stock together. It was soldered to the wings in the center of the wing (at the apex). The chord-wise dimension of the sting was 3.4 cm.

These experiments revealed a number of unique flow features for low Re swept wings, and a full report is given in appendix A. The most relevant result for the current study is that an LEV was formed with the 60° swept wing at $\alpha = 15$, 18, and 20°, shown as a sketch in figure 5.13. There are two types of LEV, and the first type is shown in figure 5.13(a). This LEV travels parallel to the leading edge, and the vortex helix angle is less than $45°$. The second case begins to develop in figure 5.13(b), and is apparent in figure 5.13(c). This LEV travels at an angle somewhere between the leading edge and the free-stream velocity. The vortex helix angle is greater than $45°$. Images and videos will be presented to justify the sketches.

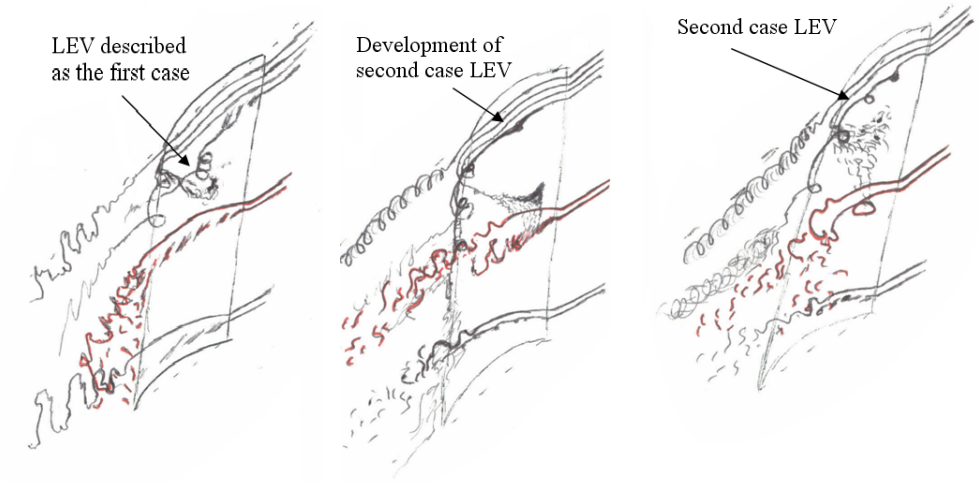

(a) $\alpha = 15°$ (b) $\alpha = 18°$ (c) $\alpha = 20°$

Figure 5.13: Sketches of Dye Visualization Experiments
These sketches show the qualitative flow patterns around the 60° swept wing at Re $= 5 \times 10^3$. The dotted line at the top represents the wing center, or the plane of symmetry of the wing. Dye streaks are drawn at three span-wise locations, and each span-wise location has several different heights above the wing drawn. At any given span-wise location, different stream tubes will illustrate different parts of the flow field depending on how far it is from the surface (ie. how much it is effected by the boundary layer and separation).

Chapter 6

Research Plan

A survey of the forces generated by 3 airfoil shapes has been conducted. A flat plate, cambered plate, and Eppler 387 (E387) airfoil has been tested at Re $= 1 \times 10^4$ and 2×10^4. Aspect ratio 6 wings were tested, and end plates were used to test 2D conditions. The following questions still need to be answered:

- How do the current measurements of flat plates and cambered plates compare to previous measurements, computational results, and analytic predictions?
- Do potential flow theories (like Thin Airfoil Theory, Lifting Line Theory, etc) apply at these Re?

Measurements of the E387 airfoil have been conducted at Re =1, 2, 3, and 6 $\times 10^4$. Previous measurements indicate that the E387 airfoil has a critical Re range near 6×10^4. Current measurements indicate that Re $= 1 \times 10^4$ and 2×10^4 are below its critical Re range. This is the first study to accurately measure a detailed drag polar for an airfoil below and within its critical Re range. At Re $= 6 \times 10^4$, the current measurements and previous measurements are in good agreement. Together, the current and previous measurements detail how the forces generated by the E387 airfoil change throughout its critical Re range. The following questions still need to be answered:

- At what Re does the discontinuity in the drag polar form? Does it form gradually, or is there a sudden appearance?
- Does the small wing produce the same drag polar as the large wing at the same Re?

The peculiar drag polar in the critical Re range has been attributed to the formation of an LSB. In particular, it is claimed that the drag increase at moderate lift coefficients is caused by the formation of an LSB, and the subsequent decrease in drag at higher α is caused by the breakdown of the LSB. However, there has been no detailed measurement of this bubble at the conditions where this drag increase occurs. In light of the drag measurements made at lower Re, there is a new possible explanation. The following questions still need to be answered:

- At what Re and α does an LSB exist for the E387 airfoil? How does this correlate to the peculiarities of the drag polar for this airfoil? Does the LSB cause the drag increase at moderate lift coefficients seen on the E387 airfoil at Re $= 6 \times 10^4$?
- What is the size, shape, and vorticity of the LSB? Can computations adequately compute this?

A swept cambered airfoil at low Re has been claimed to generate an LEV. This LEV may cause an increase in lift or a decrease in drag capable of improving the performance of small birds. However, no study has been done to identify the effects of sweep on the forces generated or on the formation of an LEV. A possible LEV has been measured in the current study that used a simple rectangular wing with sweep. The wing had no spanwise variations, and while varying the sweep, no other parameter was changed.

- How large is the LEV for a simple swept wing at low Re? What are the vorticity and circulation magnitudes?
- What are the forces generated by a simple swept wing at low Re? How does the formation of an LEV effect these forces?

The following is a detailed description of the work that will be done to answer these questions.

6.1 Force Measurements

Previous measurements of flat plates and cambered airfoils at Re $< 10^5$ can be compared to the current measurements. Also, using the Blasius boundary layer, the theoretical drag of a flat plate can be calculated and compared to current measurements. Also, computational techniques, such as Xfoil, can be used for comparison.

Thin airfoil theory and lifting line theory have been used for nearly a century, and have helped build large scale aircraft. Whether or not these potential flow theories apply below an airfoil's critical Re is still undetermined. The current measurements are the most detailed force measurements done at these Re, and should help answer this question.

6.2 Eppler 387 Performance

Force measurements will be made on the small E387 wing at $2 \times 10^4 <$ Re $< 3 \times 10^4$ to determine with more resolution where the discontinuities begin. For time considerations, the Re where the discontinuities begin will be determined with a resolution of 10^3.

A comparison between the two wings must be made. This comparison will be done at Re = 4×10^4 where the LSB is most likely a dominant feature of the flow, and is not extremely sensitive to small variations in geometry or roughness. Once the data has been taken, a measure of the deviation between the drag polar of the two wings will be made.

6.3 Laminar Separation Bubble

High resolution PIV data must be taken on the E387 airfoil to resolve the LSB. The LSB on a SD7003 airfoil measured by Radespiel et al had a height of approximately 5% of the chord. [31] Thus, for the future measurements on the large E387 wing (9 cm chord), the bubble will likely be 4 mm in height. Using a 200 mm focal length lens gives a viewing area of 1 cm-by-1 cm, and the CIV algorithm should be able to reconstruct the flow fields with 3 vectors per mm. The time between images will be approximately 16 μs. These parameters should allow for adequate resolution of the LSB. This high resolution data will be obtained at α = 1, 3, 5, 7, 10, and 13° for the Re $= 6 \times 10^4$. These represent points that cover the range where the lift and drag coefficient deviate from linear, and particularly the regions before, during and after the drag increase at moderate lift coefficients. This should clearly show how the LSB is affecting the forces generated at these low Re.

Once the data has been obtained, a time-average flow field can be constructed. Numerous velocity fields will be obtained at each α to ensure the convergence of turbulence statistics. The time-average flow should have stream lines that separate and reattach to the upper surface and turbulent shear stress that grows near the end of the bubble, similar to figure 1.13.

6.4 Leading Edge Vortex

Studies of the LEV will be made in the wind tunnel. A new 60° swept wing model, identical in geometry to the water channel experiments, will be made. The new wing will need to be smaller than the wings used in the water channel to conduct the tests at the same Re. The formation of the LEV will be investigated near $\alpha = 15°$, and PIV

data will be collected. Force measurements will also be made with the force balance at $-10^\circ < \alpha < 20^\circ$ to determine how the LEV effects the forces generated by the wing.

Chapter 7

Time Line

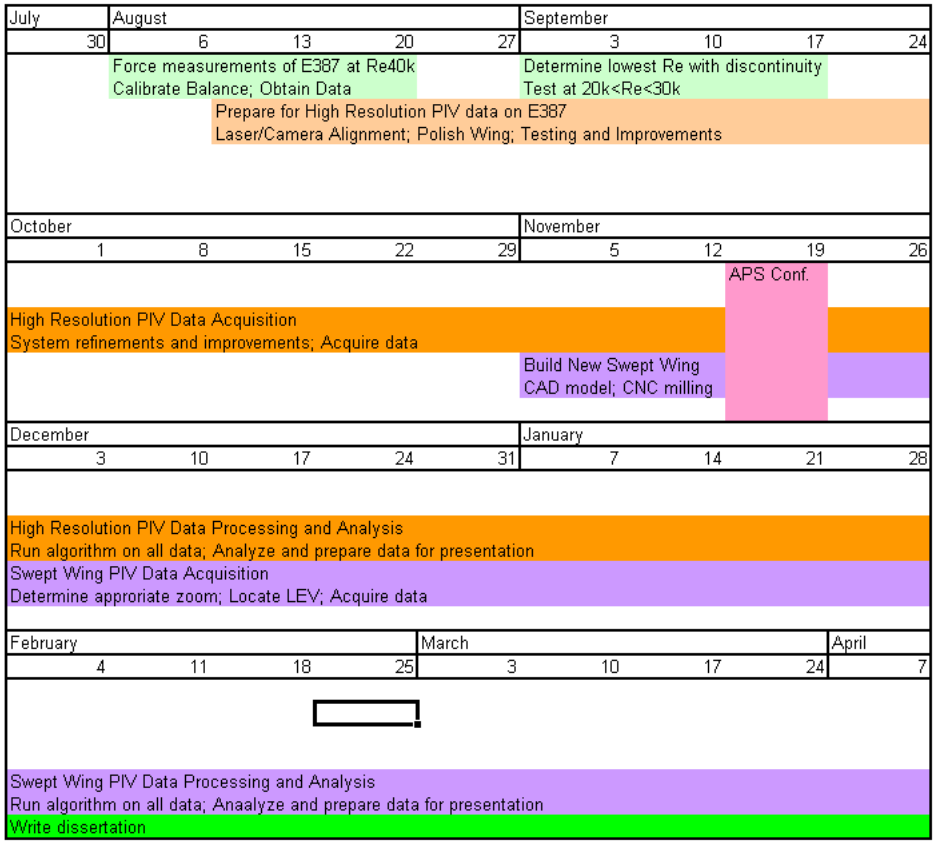

Figure 7.1: Timeline

Reference List

[1] ABBOTT, I. H., AND VON DOENHOFF, A. E. *Theory of Airfoil sections*. Dover, New York, 1959.

[2] ABBOTT, I. H., VON DOENHOFF, A. E., AND L. S. STIVERS, J. Summary of airfoil data. *NACA Technical Report 824* (1945).

[3] ALTHAUS, D. *Profilparen fur den Modellflug. Windkanalmessungen an Profilen im kritischen Reynoldszahlbereich. (Profile Polars for Model Flight. Wind-Tunnel Measurements on Profiles in the Critical Reynolds Number Range.)*. Neckar-Verlag, VS-Villingen, 1980.

[4] ALTHAUS, D., AND WORTMANN, F. X. *Stuttgarter profilkatalog I - Experimental results for the laminar wind tunnel of the University of Stuttgart*. Friedr. Vieweg and Sohn, Braunschweig, 1972 (English version in 1981).

[5] ARENA, A. V., AND MUELLER, T. J. Laminar separation, transition, and turbulent reattachment near the leading edge of airfoils. *AIAA Journal 18*, 7 (1980), 747–753.

[6] BRENDEL, M., AND MUELLER, T. J. Boundary layer measurements on an airfoil at a low Reynolds number in an oscillating freestream. *AIAA Journal 26*, 3 (1988), 257–263.

[7] BROEREN, A. P., AND BRAGG, M. B. Flowfield measurements over an airfoil during natural low-frequency oscillations near stall. *AIAA Journal 37*, 1 (1998), 130–132.

[8] BROEREN, A. P., AND BRAGG, M. B. Unsteady stalling characteristics of thin airfoils at low Reynolds number. In *Proc. Conf. on Fixed, Flapping and Rotary Wing Vehicles at Very Low Reynolds Numbers* ((Notre Dame, Ind., June, 2000 2000), pp. 396–420.

[9] DICKINSON, M. H., LEHMANN, F. O., AND SANE, S. P. Wing rotation and the aerodynamic basis for insect flight. *Science 284* (1999), 1954–1960.

[10] ELLINGTON, C. P., VAN DEN BERG, C., WILLMOTT, A. P., AND THOMAS, A. L. R. Leading-edge vortices in insect flight. *Nature 384* (1996), 626–630.

[11] FINCHAM, A. M., AND SPEDDING, G. R. Low cost, high resolution DPIV for measurement of turbulent fluid flow. *Experiments in Fluids*, 23 (1997), 449–462.

[12] GRASMEYER, J. M., AND KEENON, M. T. Development of the black widow micro air vehicle. AIAA Aerospace Sciences Meeting and Exhibit, Jan 2001.

[13] GRUNDY, T. M., KEEFE, G. P., AND LOWSON, M. V. Effects of acoustic disturbances on low re aerofoil flows. In *Proc. Conf. on Fixed, Flapping and Rotary Wing Vehicles at Very Low Reynolds Numbers* (Notre Dame, Ind., June, 2000 2000), pp. 91–113.

[14] GYLLHEM, D., MOHSENI, K., AND LAWRENCE, D. Numerical simulation of flow around the colorado micro aerial vehicle. 35th AIAA Fluid Dynamics Conference and Exhibit, June 2005.

[15] HOERNER, S. F., AND BORST, H. B. *Fluid Dynamic Lift*. Hoerner Fluid Dynamics, Bricktown, NJ, 1975.

[16] JACOBS, E. N., AND SHERMAN, A. Airfoil section charactersitcs as affected by variations of the Reynolds number. *NACA Technical Report 586* (1937).

[17] KESTER, W. ADC input noise: The good, the bad, and the ugly. Is no noise good noise? *Analog Dialogue 40*, 02 (2006). http://www.analog.com/analogdialogue.

[18] LAITONE, E. V. Wind tunnel tests of wings at Reynolds numbers below 70000. *Experiments in Fluids 23* (1997), 405–409.

[19] LENTINK, D., MULLER, U. K., STAMHUIS, E. J., DE KAT, R., GESTREL, W. V., VELDHUIS, L. L. M., HENNINGSSON, P., HEDENSTROM, A., VIDELER, J. J., AND VAN LEEUWEN, J. L. How swifts control their glide performance with morphing wings. *Nature 446* (2007), 1082–1085.

[20] LIGHTHILL, M. J. On the weis-fogh mechanism of lift generation. *JFM 60*, 1 (1973), 1–17.

[21] LISSAMAN, P. B. S. Low-Reynolds-number airfoils. *Annual Review of Fluid Mechanics 15* (1983), 223–239.

[22] LYON, C. A., BROEREN, A. P., GIGUERE, P., GOPALARATHNAM, A., AND SELIG, M. S. *Summary of Low-Speed Airfoil Data vol. 3*. SoarTech Publications, Virginia Beach, Virginia, 1996.

[23] MCGHEE, R. J., JONES, G. S., AND JOUTY, R. Performance charactersitics from wind-tunnel tests of a low-Reynolds-number airfoil. AIAA 26th Aerospace Sciences Meeting, January 1988.

[24] MCMASTERS, J. H., AND HENDERSON, M. L. Low-speed single-element airfoil synthesis. *Technical Soaring 4*, 2 (1979), 1–21.

[25] MUELLER, T. J., AND BATILL, S. M. Experimental studies of separation on a two-dimensional airfoil at low Reynolds numbers. *AIAA Journal 20*, 4 (1982), 457–463.

[26] MUELLER, T. J., AND DELAURIER, J. D. Aerodynamics of small vehicles. *Annual Review of Fluid Mechanics 35* (2003), 89–111.

[27] OL, M. V., MCAULIFFE, B. R., HANFF, E. S., SHOLZ, U., AND KAHLER, C. Comparison of laminar separation bubble measurements on a low Reynolds number airfoil in three facilities. 35th AIAA Fluid Dynamics Conference and Exhibit, June 2005.

[28] PELLETIER, A., AND MUELLER, T. J. Low Reynolds number aerodynamics of low-aspect-ratio, thin/flat/cambered-plate wings. *Journal of Aircraft 37*, 5 (2000), 825–832.

[29] PELLETIER, A., AND MUELLER, T. J. Effect of endplates on two-dimensional airfoil testing at low Reynolds number. *Journal of Aircraft 38*, 6 (2001), 1056–1059.

[30] RADESPIEL, R., WINDTE, J., AND SCHOLZ, U. Numerical and experimental flow analysis of moving airfoils with laminar separation bubbles. 44th AIAA Aerospace Sciences Meeting and Exhibit, Jan 2006.

[31] RADESPIEL, R., WINDTE, J., AND SCHOLZ, U. Numerical and experimental flow analysis of moving airfoils with laminar separation bubbles. *AIAA Journal 45*, 6 (2007), 1346–1356.

[32] RIEGELS, F. W. *Airfoil sections*. Butterworth, London, 1961.

[33] SCHLICTING, H., AND GERSTEN, K. *Boundary Layer Theory*. Springer-Verlag, Berlin, Germany, 2003.

[34] SCHMITZ, F. W. *Aerodynamik des Flugmodells*. C. J. E. Volckmann Nachf. E. Wette, Berlin-Charlottenburg, 1942.

[35] SELIG, M. S., DONOVAN, J. F., AND FRASER, D. B. *Airfoils at Low Speeds*. H.A. Stokely, Virginia Beach, Virginia, 1989.

[36] SELIG, M. S., GUGLIELMO, J. J., BROEREN, A. P., AND GIGUERE, P. *Summary of Low-Speed Airfoil Data vol. 1*. SoarTech Publications, Virginia Beach, Virginia, 1995.

[37] SELIG, M. S., LYON, C. A., GIGUERE, P., NINHAM, C. P., AND GUGLIELMO, J. J. *Summary of Low-Speed Airfoil Data vol. 2*. SoarTech Publications, Virginia Beach, Virginia, 1996.

[38] SELIG, M. S., AND MCGRANAHAN, B. D. Wind tunnel aerodynamic tests of six airfoils for use on small wind turbines. *Transactions of the ASME 126* (2004), 986–1001.

[39] SRYGLEY, R. B., AND THOMAS, A. L. R. Unconventional lift-generating mechanisms in free-flying butterflies. *Nature 420* (2002), 660–664.

[40] VIDELER, J. J., STAMHUIS, E. J., AND POVEL, G. D. E. Leading-edge vortex lifts swift. *Science 306* (2004), 1960–1962.

[41] VOLKERS, D. F. Preliminary results of windtunnel measurements on some airfoil sections at Reynolds numbers between 0.6×10^4 and 5.0×10^5. Internal Memorandum: M-276, http://home.hccnet.nl/d.f.volkers/m276.ppt, June 1977.